The Journal of Organic Chemistry

Subscriber access provided by Uppsala universitetsbibliotek

Article

The Electrochemically Catalyzed Newman-Kwart Rearrangement: Mechanism, Structure-Reactivity Relationship, and Parallels to Photoredox Catalysis

Arend F. Roesel, Mihkel Ugandi, Nguyen Thi Thu Huyen, Michal
Majek, Timo Broese, Michael Roemelt, and Robert Francke

J. Org. Chem., **Just Accepted Manuscript** • DOI: 10.1021/acs.joc.0c00831 • Publication Date (Web): 26 May 2020

Downloaded from pubs.acs.org on May 28, 2020

Just Accepted

“Just Accepted” manuscripts have been peer-reviewed and accepted for publication. They are posted online prior to technical editing, formatting for publication and author proofing. The American Chemical Society provides “Just Accepted” as a service to the research community to expedite the dissemination of scientific material as soon as possible after acceptance. “Just Accepted” manuscripts appear in full in PDF format accompanied by an HTML abstract. “Just Accepted” manuscripts have been fully peer reviewed, but should not be considered the official version of record. They are citable by the Digital Object Identifier (DOI®). “Just Accepted” is an optional service offered to authors. Therefore, the “Just Accepted” Web site may not include all articles that will be published in the journal. After a manuscript is technically edited and formatted, it will be removed from the “Just Accepted” Web site and published as an ASAP article. Note that technical editing may introduce minor changes to the manuscript text and/or graphics which could affect content, and all legal disclaimers and ethical guidelines that apply to the journal pertain. ACS cannot be held responsible for errors or consequences arising from the use of information contained in these “Just Accepted” manuscripts.

is published by the American Chemical Society. 1155 Sixteenth Street N.W.,
Washington, DC 20036

Published by American Chemical Society. Copyright © American Chemical Society.
However, no copyright claim is made to original U.S. Government works, or works
produced by employees of any Commonwealth realm Crown government in the course
of their duties.

The Electrochemically Catalyzed Newman-Kwart Rearrangement: Mechanism, Structure-Reactivity Relationship, and Parallels to Photoredox Catalysis

Arend F. Roesel,[1] Mihkel Ugandi,[2] Nguyen Thi Thu Huyen,[1,3] Michal Májek,[1,4] Timo Broese,[1] Michael Roemelt,[2,*] and Robert Francke[1,*]

[1] Institute of Chemistry, Rostock University, Albert-Einstein-Str. 3a, 18059 Rostock, Germany.
[2] Chair for Theoretical Chemistry, Ruhr-University Bochum, 44780 Bochum, Germany.
[3] School of Chemical Engineering, Hanoi University of Science and Technology, 1 Dai Co Viet Road, Hanoi, Vietnam
[4] Department of Organic Chemistry, Faculty of Natural Sciences, Comenius University in Bratislava, Mlynská dolina, Ilkovičova 6, 84215 Bratislava, Slovakia.

Electrosynthesis – Catalysis – Molecular Rearrangement – Thiophenol – Cyclic voltammetry

ABSTRACT: The facilitation of redox-neutral reactions by electrochemical injection of holes and electrons, also known as 'electrochemical catalysis', is a little explored approach that has the potential to expand the scope of electrosynthesis immensely. To systematically improve existing protocols and to pave the way toward new developments, a better understanding of the underlying principles is crucial. In this context, we have studied the Newman-Kwart rearrangement of *O*-arylthiocarbamates to the corresponding *S*-aryl derivatives, the key-step in the synthesis of thiophenols from the corresponding phenols. This transformation is a particularly useful example, since the conventional method requires temperatures up to 300 °C, whereas electrochemical catalysis facilitates the reaction at room temperature. A combined experimental-quantum chemical approach revealed several reaction channels and rendered an explanation for the relationship between structure and reactivity. Furthermore, it is shown how rapid CV measurements can serve as a tool to predict the feasibility for specific substrates. The study also revealed distinct parallels to photoredox-catalyzed reactions, in which back-electron transfer and chain propagation are competing pathways.

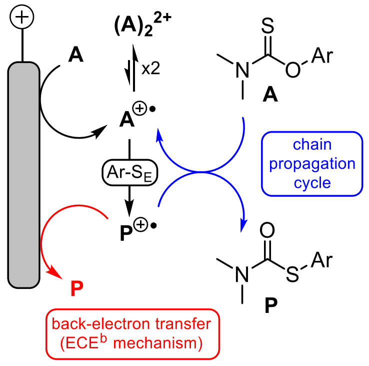

Introduction.

The vast majority of the electro-organic conversions reported in the literature are redox reactions which involve either the transformation of functional groups or the formation (and cleavage, respectively) of chemical bonds.[1–7] As a consequence, at least stoichiometric amounts of electric charge are required to achieve a full conversion. Very few reported examples, however, show that sub-stoichiometric amounts can be used to facilitate overall redox-neutral chemical reactions.[8] This scenario is denoted as 'electrochemical catalysis' and is triggered by the electrochemical generation of an ionic or radical ionic species.[8,9] After a coupled chemical step, the reaction sequence is either terminated by a backward electron exchange with the electrode (ECE^b mechanism) or a chain process is initiated in the bulk solution. Under these conditions, sub-stoichiometric charge quantities are sufficient for a full conversion, and conceptually the injected electrons and holes can be regarded as catalysts. The feasibility of this approach for electrolysis on a preparative scale has been demonstrated several times in the past, e.g. with hole-induced cycloadditions[10–13] and molecular rearrangements,[14,15] as well as with electron-catalyzed $S_{RN}1$ reactions.[16,17]

The utility of the concept is particularly well illustrated by the Newman-Kwart rearrangement of *O*-aryl thiocarbamates **2** to the corresponding *S*-aryl compounds **3**, which represents the key-step in the synthesis of thiophenols **4** from phenols **1** (see Scheme 1).[18] Traditionally, the NKR is carried out at temperatures between 200 and 300 °C,[19] which has been rationalized by the rearrangement following an intramolecular ArS_N mechanism passing through the strained spirocyclic structure **TS-1**.[20] In recent decades, non-electrochemical approaches toward enabling a transformation under milder conditions have been developed. These advancements include improved heat transfer by microwave-irradiation[21-23] as well as decreasing the required temperature by using stoichiometric amounts of $BF_3{\cdot}OEt_2$[24] or catalytic amounts of $[Pd(tBu_3P)_2]$.[25] More recently, it was shown that the *O*,*S*-rearrangement can be achieved at room temperature by irradiation with blue light in presence of a pyrylium-based photoredox catalyst[26] or by treatment with chemical oxidants.[27,28] Electrochemical catalysis, however, allows for additive-free reaction at room temperature, which was demonstrated by a synthetic study carried out in our laboratory (Scheme 1, bottom).[15]

SCHEME 1. Synthesis of thiophenols 4 from phenols 1 via the thermal and the electrochemical NKR route, respectively.

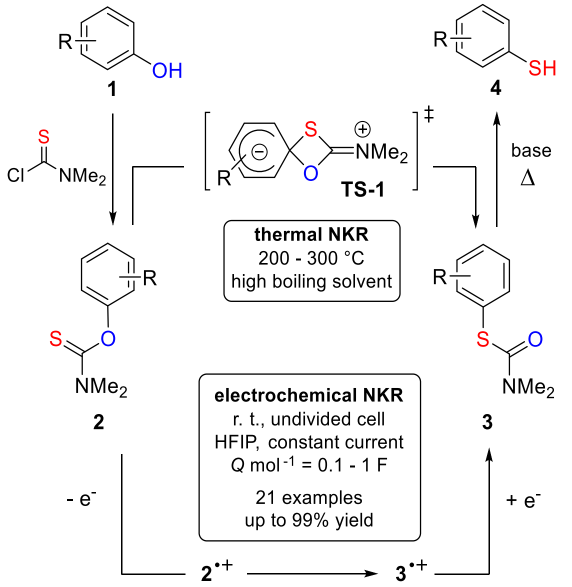

The electrochemical method (ENKR) is characterized by a simple set-up (galvanostatic conditions, undivided cell, carbon anode), good scalability, short reaction times and good to excellent yields in compounds of type **3**. While for the batch process, NBu_4ClO_4 was used as a supporting electrolyte, we have shown that the use of a microflow cell allows for salt-free electrolysis on the gram-scale, rendering the products in quantitative yield and analytical purity after recovery of the solvent without further purification. Noteworthy, the use of 1,1,1,3,3,3-hexafluoroisopropanol (HFIP) as solvent is crucial, since other solvents either decrease the yields or completely inhibit the rearrangement.

In contrast to the thermal NKR, where electron-deficient aromatics react faster than electron-rich ones,[29] we found that the room temperature ENKR exhibits an inverted reactivity trend. On the basis of this observation and in agreement with the abovementioned examples where the NKR was induced by non-electrochemical oxidation,[26-28] we have proposed the mechanistic rationale shown in Scheme 1.[15] The sequence is initiated by anodic generation of **2**$^{\bullet+}$, followed by rearrangement to **3**$^{\bullet+}$ and reduction either by the anode (ECE[b]) or by **2** (chain process).

While electrocatalysis (which is generally understood as the facilitation of the heterogeneous electron exchange via a chemical interaction between the substrate and an electrocatalyst) is well understood,[30-34] only few detailed studies of electrochemically catalyzed reactions are available.[35] Since electrochemical catalysis has the potential to massively expand the scope of electrosynthesis, we believe that a better mechanistic understanding including the knowledge about preconditions and typical bottlenecks is the key to the successful development of similar transformations in the future. We have therefore carried out a detailed study of the ENKR using both experimental and quantum chemical methods, the results of which are presented herein.

Results and Discussion.

The molecularity of the electrochemical NKR. We started our study with an investigation of the molecularity of the rearrangement. In principle, a mono- and a bimolecular pathway are conceivable (see Scheme 2). The monomolecular pathway proceeds via spirocyclic intermediate **TS-2** as previously proposed for the photoredox-catalytic NKR.[26] Analogously, the ENKR is initiated by oxidation of **2**. However, the heterogeneous electron transfer leads to a local accumulation of **2a**$^{\bullet+}$ close to the electrode surface**,** whereas the concentration of the reactive intermediate is spatially independent when a homogeneous oxidant is used. Therefore, we have also taken into account a bimolecular pathway, which passes through eight-membered **TS-3**.[36] A bimolecular process via a charge-neutral **TS-3**-type transition-state has initially been proposed for the thermal (microwave-assisted) NKR at high concentrations,[37] which was later conclusively disproven.[38]

SCHEME 2. Possible pathways for the rearrangement 2$^{\bullet+}$ **→ 3**$^{\bullet+}$**.**

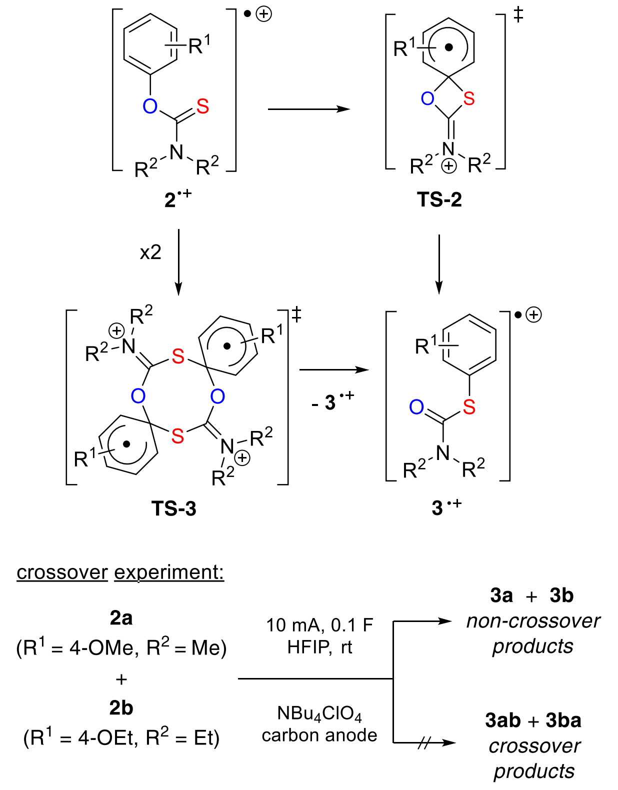

To investigate whether the rearrangement proceeds in an intra- or in an intermolecular fashion, we have carried out a crossover experiment between the 4-methoxy-*N*,*N*-dimethyl substituted species **2a** and its 4-ethoxy-*N*,*N*-diethyl derivative **2b** under standard electrolysis conditions. After passing 0.1 F with respect to **2a** and **2b**, full conversion into **3a** and **3b** was achieved, whereas no crossover products were observed (for more details see the Supporting Information, SI). It can therefore be concluded that under standard electrolysis conditions, the rearrangement proceeds via the intramolecular pathway.

Voltammetric analysis. With the goal to collect mechanistic proof and to devise a diagnostic criterion for the feasibility of the ENKR for specific substrates, we carried out cyclic voltammetry (CV) with initially three representatives of the *O*-aryl thiocarbamates in 0.1 M NBu_4BF_4/HFIP. Two of these examples, **2a** (R = 4-OMe) and **2e** (R = 4-NHAc), belong to the group of ENKR-susceptible compounds, while **2t** (R = 4-F) does not rearrange under standard electrolysis conditions.[15] In Figure 1, the CVs of **2** (solid line) are depicted along with the CVs of the corresponding *S*-aryl derivatives **3** (dashed line).

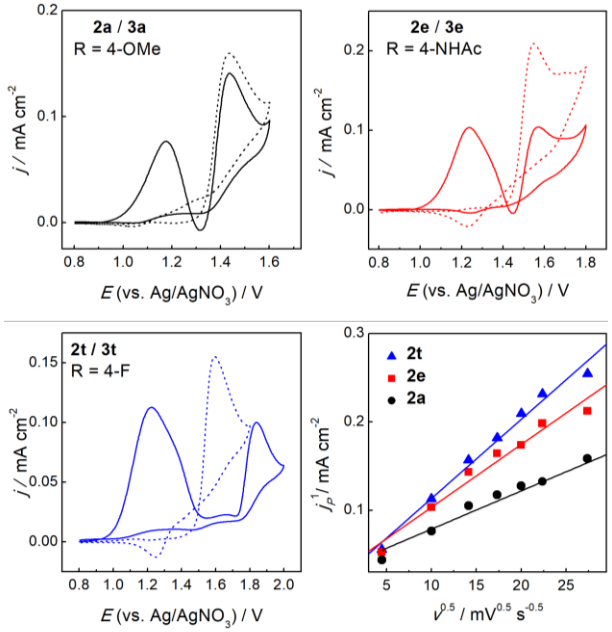

Figure 1. Top and bottom left: Background-corrected voltammetric responses of three *O*-arylthiocarbamates **2** (solid lines) and their *S*-aryl derivatives **3** (dashed lines) in 0.1 M NBu_4BF_4/HFIP (v = 100 mV s^{-1}, c(**2**) = c(**3**) = 1 mM, working electrode: glassy carbon). Bottom right: Plot of the peak current densities (j_P^1) vs. $v^{1/2}$.

The scan of the positive potential regime of the 4-methoxy substituted compound **2a** at v = 100 mV s^{-1} exhibits two irreversible signals with peak potentials at $E_P^1(\mathbf{2a})$ = 1.18 V and $E_P^2(\mathbf{2a})$ = 1.44 V (top left, solid black line). While the shape of the second signal resembles the one of a typical EC process,[39] the first signal appears rather unusual. An uncommon feature is that the peak current density of the first signal $j_P^1(\mathbf{2a})$ is relatively low compared to the one of the second $j_P^2(\mathbf{2a})$. Furthermore, after passing through $E_P^1(\mathbf{2a})$, the profile does not converge against the diffusion-limited current, but decreases continuously until reaching a negative "dip" at approx. 1.32 V. Before discussing the origin of the unusual behavior, it is useful to assign the individual features to the associated electrochemical processes. For this assignment a comparison with the CV of the corresponding *S*-arylthiocarbamate **3a** is helpful (dashed black line), which exhibits only a single feature at $E_P^1(\mathbf{3a})$ = 1.44 V in the scanned potential regime. Since the second anodic peak in the CV of **2a** appears at exactly this potential in a similar shape, a mechanism that explains the voltammetric behavior can be derived (Figure 2, top). Thus, oxidation at $E_P^1(\mathbf{2a})$ leads to formation of $\mathbf{2a}^{\bullet+}$, which spontaneously rearranges to $\mathbf{3a}^{\bullet+}$, followed by reduction to **3a** either via backward electron transfer (BET) from the electrode or via a chain process. Then, upon reaching $E_P^2(\mathbf{2a})$, *in situ* formed **3a** is reoxidized to $\mathbf{3a}^{\bullet+}$. The digital simulation of the anodic scan confirms that an explanation of the signature profile is possible based on the proposed kinetic model (Figure 2, bottom, for more details regarding parameters and v- dependency see the SI). For an accurate fitting to the full CV, an extended model is required, which will be discussed later.

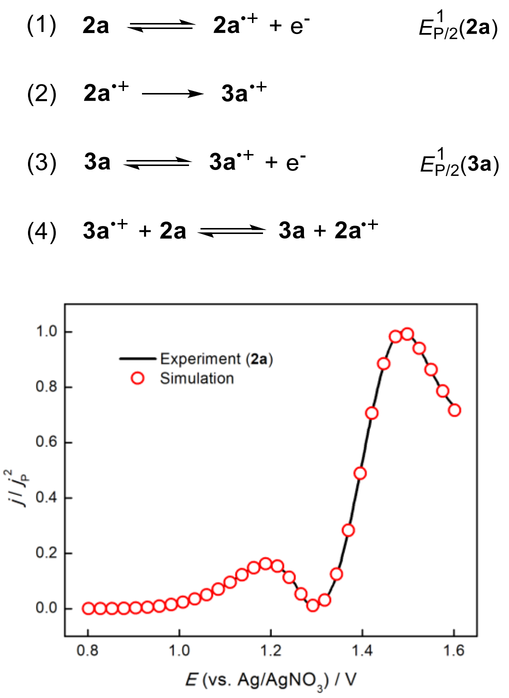

Figure 2. Top: Chemical and electrochemical steps that account for the features of the anodic scan of **2a**. Bottom: Digital simulation (red circles) of the normalized current profile (solid line) using eqs. 1-4 (v = 400 mV s^{-1}, 5 mM **5a**). The simulations were carried out using the DigiElch package.[40]

Since the peak associated with the re-oxidation is similarly pronounced as the anodic peak in the CV of **3a**, it can be assumed that upon passing through $E_P^2(\mathbf{2a})$, most of the *O*-arylthiocarbamate molecules near the electrode are already rearranged to the corresponding *S*-aryl derivative. The fact that $j_P^1(\mathbf{2a})$ is much smaller than $j_P^2(\mathbf{2a})$ can indicate both that a part of the oxidative current is quenched by simultaneous BET and that the concentration of redox-active **2a** in the vicinity of the electrode is diminished by a radical chain process migrating from the electrode surface into the solution (*vide infra*).

With two irreversible signals at $E_P^1(\mathbf{2e})$ = 1.24 V and $E_P^2(\mathbf{2e})$ = 1.57 V, respectively, the anodic scan of the 4-acetamido substituted thiocarbamate **2e** exhibits similar characteristics (Figure 1, top right). Again, $E_P^2(\mathbf{2e})$ matches the peak potential of the corresponding *S*-aryl ($E_P^1(\mathbf{3e})$ = 1.55 V). In contrast to **2a**, however, the ratio between $j_P^1(\mathbf{2e})$ and $j_P^2(\mathbf{2e})$ is approx. one, while $j_P^2(\mathbf{2e})$ only reaches about 50% of $j_P^1(\mathbf{3e})$. From the latter observation it can be concluded that the *O*-aryl compounds are only partially converted upon reaching E_P^2(**2e**) and consequently, that the rate of the step $\mathbf{2e}^{\bullet+}\rightarrow\mathbf{3e}^{\bullet+}$ must be significantly smaller than for $\mathbf{2a}^{\bullet+}\rightarrow\mathbf{3a}^{\bullet+}$.

Compared to **2a** and **2e**, the behavior of **2t** is fundamentally different (Figure 1, bottom left). While the anodic scan again exhibits two features with E_P^1(**2t**) = 1.22 V and E_P^2(**2t**) = 1.84 V, the second peak potential does not match the peak potential of the *S*-aryl derivative (E_P^1(**3t**) = 1.60 V). From this mismatch, it can be concluded that anodically generated $\mathbf{2t}^{\bullet+}$ does not rearrange to $\mathbf{3t}^{\bullet+}$. These results are in agreement with the outcome of the preparative-scale electrolysis of **2t**, where the formation of **3t** was not observed.[15] The irreversibility of the peak at 1.22 V, indicates that another chemical step is coupled to the initial electron transfer.[41] Thus, j_P^2(**2t**) must originate from oxidation of another intermediate than $\mathbf{2t}^{\bullet+}$ or **3t**. A plausible explanation is that oxidation at E_P^1(**2t**) leads to desulfurization and thus to formation of the carbamate (**5t**), which would be oxidized at 1.84 V. To probe this possibility, we have carried out CV with an authentic sample of **5t**. Since E_P^1(**5t**) amounts to 2.04 V, the occurrence of carbamate **5t** in the anodic scan of **2t** can be excluded. The absence of a carbamate species was confirmed in the same way for the anodic scan of 4-Cl substituted compound **2v** (the CVs of **5t** and **5v** are shown in the SI).

Due to the fact that oxidation of **2t** cannot trigger ECE^b or chain processes, it is safe to assume that j_P^1 is merely diffusion-limited and exhibits Randles-Sevcik behavior,[42] which is in agreement with the linear relationship to $v^{1/2}$ (Figure 1, bottom right). For **2a** and **2e**, the plot $j_P^1 \rightarrow v^{1/2}$ also exhibits linearity, albeit with a significantly smaller slope. The smaller slopes indicate that the ECE^b and/or the chain process are additional j_P-limiting factors. The observed decrease of the slope in the order **2t** > **2e** > **2a** can thus be used for a qualitative assessment for the rate of the rearrangement step.

Noteworthy, the CVs of **3a**, **3e** and **3t** have an unusual crossing between the profile lines of the forward and the backward scan in common (1.3 - 1.5 V). This is a typical sign for the redox process leading to a product, which is easier to oxidize than the starting material. This feature will be discussed later in more detail.

To find out how other representatives of **2** and **3** behave under these conditions, we have carried out CV studies with a set of 25 differently substituted *O*-arylthiocarbamates in a NBu_4BF_4/HFIP electrolyte (see Table 1). Based on our previous synthetic study[15] and several additional preparative-scale experiments (see the SI), these compounds can be divided in two groups, those that are susceptible to the ENKR (**2a – 2r**, slow NKR of **2q** and **2r** at room temperature) and those that are non-reactive under standard electrolysis conditions (**2s – 2x**). Interestingly, the diagnostic criteria described for **2a**, **2e** and **2t** seem to be generalizable, since all of the studied ENKR-susceptible compounds exhibit the same characteristics as **2a**/**3a** and **2e**/**3e**, while all of the non-reactive congeners follow the same trend as **2t**/**3t** (see the SI). CV can thus be considered as a straightforward and rapid tool to assess the feasibility of the ENKR for particular compounds **2**.

Table 1. Peak potentials (E_P) and half-wave potentials ($E_{P/2}$) extracted from the CVs of 2 and 3.

	***O*-Arylthiocarbamate**	**$E_P^1(2)$ [V]**	**$E_P^2(2)$ [V]**	**$E_{P/2}^1(2)$ [V]**	**$E_{P/2}^2(2)$ [V]**	***S*-Arylthiocarbamate (isolated yield)^a**	**$E_P^1(3)$ [V]**	**$E_{P/2}^1(3)$ [V]**
Susceptible to ENKR at r. t.	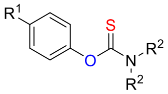					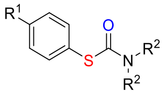		
	2a (R^1 = OMe, R^2 = Me)	1.18	1.44	1.09	1.38	**3a** (95%, >99%^{b})	1.44	1.37
	2b (R^1 = OEt, R^2 = Et)	1.15	1.39	1.07	1.33	**3b** (91%)	1.40	1.33
	2ab (R^1 = OEt, R^2 = Me)	1.18	1.42	1.09	1.36	**3ab** (80%)	1.39	1.33
	2c (R^1 = OBu, R^2 = Me)	1.18	1.41	1.09	1.35	**3c** (90%)	1.40	1.34
	2d (R^1 = SMe, R^2 = Me)	1.10	1.30	1.04	1.24	**3d** (85%)	1.29	1.24
	2e (R^1 = NHAc, R^2 = Me)	1.24	1.57	1.14	1.50	**3e** (71%)	1.55	1.49
	2f (R^1 = NHBoc, R^2 = Me)	1.22	1.48	1.11	1.41	**3f** (68%)	1.46	1.40
	2g (R^1 = OPh, R^2 = Me)	1.17	1.50	1.08	1.44	**3g** (78%)	1.50	1.44
	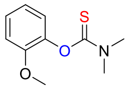					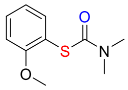		
	2h	1.21	1.54	1.11	1.48	**3h** (93%)	1.54	1.48
	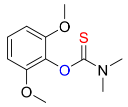					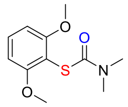		
	2i	1.21	1.49	1.08	1.44	**3i** (94%)	1.48	1.43

	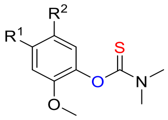					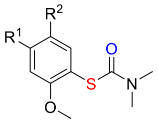		
	2j (R¹ = Me, R² = H)	1.11	1.45	0.98	1.39	**3j** (90%)	1.44	1.37
	2k (R¹ = H, R² = F)	1.21	1.61	1.12	1.54	**3k** (70%)	1.58	1.53
	2l (R¹ = allyl, R² = H)	1.20	1.45	1.11	1.41	**3l** (54%)	1.47	1.40
	2m (R1 = vinyl, R² = H)	1.21	1.40	1.11	1.35	**3m** (40%)	1.39	1.32
	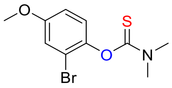					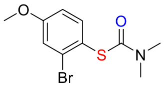		
	2n	1.20	1.55	1.09	1.50	**3n (**79%)	1.55	1.49
	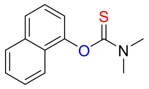					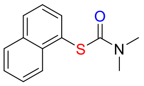		
	2o	1.20	-[f]	1.12[g]	1.46[g]	**3o** (72%)	1.52	1.44
	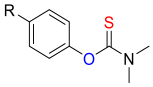					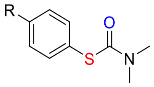		
	2p[c] (R = NMe₂)	1.21	1.59	1.21	1.53	**3p**[c] (35%, 77%[d])	1.62	1.54
ENKR only at 58 °C	**2q**[e] (R = Me)	1.21	1.66	1.13	1.60	**3q**[e] (70%)	1.64	1.58
	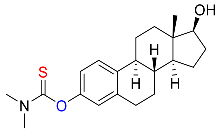					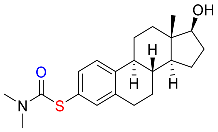		
	2r[e]	1.23	1.64	1.14	1.59	**3r**[e] (45%)	1.62	1.55
No reactivity at 58 °C	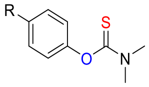					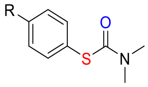		
	2s (R = H)	1.24	1.92	1.14	1.87	**3s** (n. d.)	1.78	1.71
	2t (R = F)	1.22	1.84	1.10	1.78	**3t** (n. d.)	1.60	1.53
	2u (R = NO₂)	-[f]	-[h]	1.53[g]	-[h]	**3u** (n. d.)	2.12	2.03
	2v (R = Cl)	1.21	1.82	1.09	1.75	**3v** (n. d.)	1.80	1.74
	2w (R = COOMe)	1.27	-[h]	1.14	-[h]	**3w** (n. d.)	2.03	1.96
	2x (R = CF₃)	1.33	-[h]	1.14	-[h]	**3x** (n. d.)	2.05	1.97

[a] Yields of the batch processes taken from ref. 15. [b] Isolated yield under optimized flow conditions. [c] In addition to the shown values, the CV of **2p** exhibits a reversible signal centered around 0.78 V. [d] Yield of a controlled potential electrolysis determined via GC using an internal standard (see Table 4). [e] Rearrangement only under reflux conditions (bp. HFIP: 58 °C). [f] No clear resolution of the signal. [g] $E_{P/2}$ was estimated using differential pulse voltammetry (see SI). [h] No occurrence of a second signal in the scanned potential regime.

Further mechanistic information can be obtained upon variation of the concentration of **2** (see Figure 3). For **2a**, an increase from 1 mM (top left, solid line) to 7 mM (dashed line) only leads to a moderate increase of $j_P^1(\mathbf{2a})$, whereas $j_P^2(\mathbf{2a})$ grows significantly. The decrease of the ratio between $j_P^1(\mathbf{2a})$ and $j_P^2(\mathbf{2a})$ clearly indicates a growing efficiency of the radical chain process, which leads to more depletion of **2a** close to the electrode surface while increasing the concentration of **3a**. The same *c*-dependent effect, albeit less pronounced, can also be observed for **2e**, which again reflects the smaller rate for $\mathbf{2e}^{\bullet+}\rightarrow\mathbf{3e}^{\bullet+}$ compared to $\mathbf{2a}^{\bullet+}\rightarrow\mathbf{3a}^{\bullet+}$. In contrast, $j_P^1(\mathbf{2t})$ increases linearly with c (as predicted by the Randles-Sevcik equation), which is in agreement with the absence of the radical chain process.

From the dramatic effect of *c* and the minor influence of *v*, it can be concluded that the radical chain mechanism plays the more important role for sustaining the catalytic cycle compared to the ECE^b mechanism. The most obvious explanation for this is that the rearrangement $\mathbf{2}^{\bullet+}\rightarrow\mathbf{3}^{\bullet+}$ is slow enough for $\mathbf{2}^{\bullet+}$ to diffuse from the electrode surface into the solution, where the rearrangement can finally set the chain mechanism in motion.

A further important detail which becomes evident at high concentrations is the appearance of a shoulder between 1.1 V and 1.4 V during the cathodic scans of **2a** and **2e**, which leads to an unusual crossing of the profiles. Such a line crossing was already observed in the CVs of **3a**, **3e** and **3t** (*vide supra*), and further highlights the possibility that oxidation of **3** leads to a product that is easier to oxidize than the *S*-aryl compound (for details see penultimate section). A similar effect is also observed with **2t**, although the cause must obviously be different.

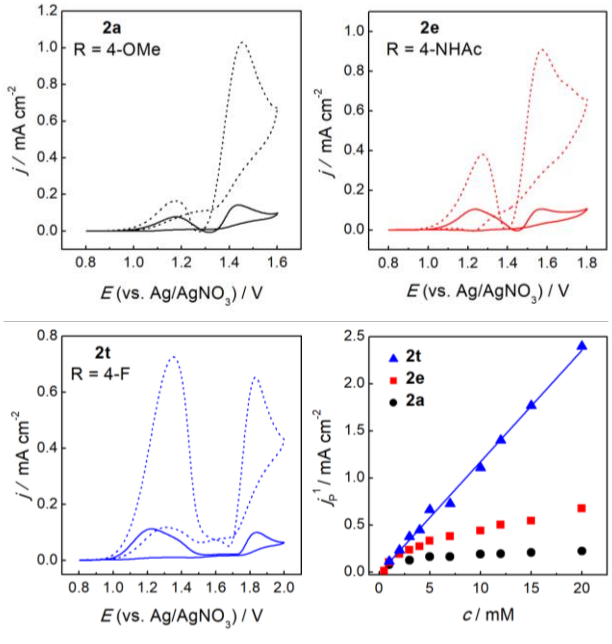

Figure 3. Influence of the concentration on the voltammetry of **2a, 2e**, and **2t**. Top and bottom left: Background-corrected voltammetric responses at 1 mM **2** (solid lines) and 7 mM **2** (dashed lines) in 0.1 M NBu_4BF_4/HFIP (v = 100 mV s^{-1}). Bottom right: Plot of the first peak current densities (j_P^1) vs. *c*.

To learn more about the relationship between the aryl substitution and the electrochemical behavior of compounds **2** and **3**, it is useful to relate the redox potentials to the electronic properties of the substituents. For this purpose, the first half-wave potentials $E^1_{P/2}$ of the *O*- and *S*-aryl compounds carrying only *para* substituents were plotted against the corresponding σ_P^+ parameters (see Figure 4).[43]

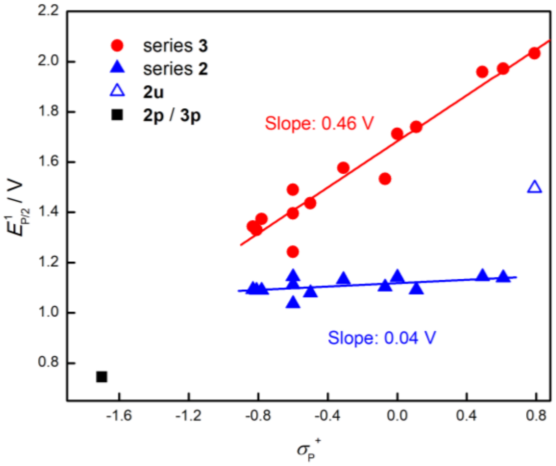

Figure 4. Plot of the first half-wave-potentials $E^1_{P/2}$ of *para*-substituted compounds **2** and **3** vs. their σ_P^+ constants.

The Hammett plot reveals several important mechanistic details. First, $E^1_{P/2}(\mathbf{2}) \geq E^1_{P/2}(\mathbf{3})$ as an important precondition for electrochemical catalysis is fulfilled in all cases,[8] even for those where the ENKR does not occur under standard electrolysis conditions. In other words, the $\mathbf{3}/\mathbf{3}^{\bullet+}$ couple constitutes a stronger oxidant than the $\mathbf{2}/\mathbf{2}^{\bullet+}$ couple, which allows the chain process (or the ECE^b mechanism) to proceed spontaneously. It can therefore be concluded that in the non-ENKR case, neither the initiation $\mathbf{2}\rightarrow\mathbf{2}^{\bullet+}$ nor the chain propagation are the prohibiting steps. Second, with the exception of **2p**/**3p** (4-R = NMe_2, $\sigma_P^+ = -1.7$) and **2u** (4-R = NO_2, $\sigma_P^+ = 0.79$) each series follows a linear trend according to equations 5 and 6.

$$(5)\quad E^1_{P/2}(\mathbf{2}) = 1.16\,V + 0.04\,V\cdot\sigma_P^+$$

$$(6)\quad E^1_{P/2}(\mathbf{3}) = 1.68\,V + 0.46\,V\cdot\sigma_P^+$$

The slope provides a measure of the influence of the substituents upon the observed potential, while the intercept refers to the oxidation potential of the unsubstituted compound of the series.[44] Compounds **2p**, **3p** and **2u** deviate from the trend and are therefore not taken into account in the equations. The voltammetric behavior of **2u** is inconclusive and different from the other non-NKR compounds of the series. The half-wave potential shown in Table 1 could only be obtained by means of differential pulse voltammetry (see the SI). While the reason for the deviation of **2u** remains unclear, the 4-NMe_2-substituted **2p**/**3p** couple assumes a special role which is discussed further below. In view of the slopes of the two linear equations, it becomes obvious that the influence of the electronic character of the substituents on $E^1_{P/2}$ is much less pronounced in the case of **2** than for **3**. This assessment is confirmed by the spin densities depicted in Figure 5 (top) that were obtained from DFT calculations. In **2** the spin is mostly sulfur-centered with only little contributions from the aromatic ring while for **3** the density is considerably shifted towards the aromatic ring. This indicates that the *O*-aryls are oxidized at the thiocarbamoyl group, while charge and spin density are predominantly localized on the aryl unit in the case of **3**. The resonance formulas that best fit this picture are shown in Figure 5 (bottom). From these observations it can also be deduced that the rearrangement of the radical cations proceeds via an intramolecular electrophilic aromatic substitution. These findings are in agreement with previous studies on the NKR induced by chemical oxidants.[45,46]

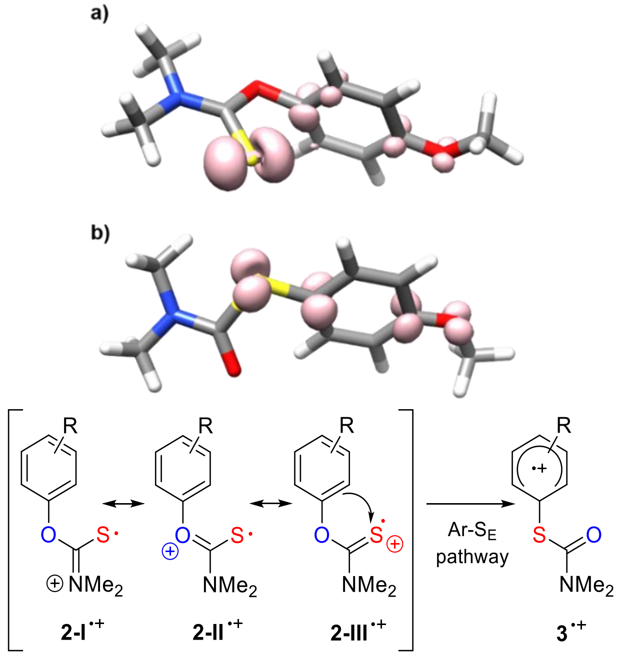

Figure 5. Top: Isosurface of the calculated spin densities of **2a**$^{+\bullet}$ (a) and **3a**$^{+\bullet}$ (b) at a value of 0.01 electron spins. In **2a**$^{+\bullet}$ the spin is mostly sulfur-centered with only little contributions from the aromatic ring while in **3a**$^{+\bullet}$ the density is considerably shifted towards the aromatic ring. Bottom: Resonance formula of **2**$^{\bullet+}$ and **3**$^{\bullet+}$ which are in best agreement with the Hammett correlation.

Relationship between arene substitution and reactivity. As discussed above, the cation radical NKR induced by chemical oxidants exhibits the same reactivity trends in terms of electron donating or withdrawing substituents as our electrochemical reaction.[26-28] While kinetic control of the overall reaction by the rearrangement was suggested,[45,46] the central mechanistic feature governing the observed behavior could not be unambiguously identified so far. The above presented analysis of our electrochemical data excludes the reactant oxidation and radical chain propagation as possible candidates. Hence the most straightforward explanation would indeed involve kinetic control by the rearrangement, i.e. that the reaction barrier for **2**$^{\bullet+} \rightarrow$ **3**$^{\bullet+}$ for compounds bearing electron withdrawing groups is significantly increased thus prohibiting product formation. However, no conclusive relation was found by quantum chemical calculations on the DFT and G4MP2 level of theory. Our electronic structure calculations at the local coupled cluster level (see computational details in experimental section) agree with these findings. Although electron withdrawing substituents in general lead to higher reaction barriers (see Figure 6, right), the trend is not sufficiently pronounced to conclusively explain the observed selectivity. Instead all calculated reaction barriers are considerably below 20 kcal mol^{-1} (see Table 2). The barriers for **2t**, **2u** and **2x** alone should thus not be prohibitive, in particular since the ENKR does not even proceed at the boiling point of HFIP (58 °C) for these substrates.

The relatively low reaction barriers point toward another reason for the lack of reactivity for electron-deficient aromatics. Since electrolysis of **2t** and **2u** under standard conditions did not lead to conversion (no consumption of starting material), off-cycle equilibria yielding stabilized intermediates were the starting point for our considerations. Recently, Nicewicz and coworkers proposed a dimerization according to

$$(7) \quad \mathbf{2a} + \mathbf{2a}^{\bullet+} \rightleftharpoons (\mathbf{2a})_2^{\bullet+}$$

as competing process that could prevent the rearrangement reaction but no experimental evidence for the exact nature of the off-cycle intermediate could be found.[46] Inspired by this idea, we studied various dimerization reactions by means of quantum chemical methods and found that while $(\mathbf{2})_2^{\bullet+}$ is not stable with respect to a decay into the monomeric species, the reaction

$$(8) \quad 2\ \mathbf{2a}^{\bullet+} \rightleftharpoons (\mathbf{2a})_2^{2+}$$

leads to a stable S-S bond (Figure 6, left) reflected by a corresponding free reaction energy of −10.8 kcal mol^{-1} for the 4-methoxy (**2a**/**3a**) derivative. This and all other free energies for dimerization reactions in Table 2 are upper bounds to the true free energies as the translational entropy contributions of the monomers on the order of 12 kcal mol^{-1} are obtained from an idealized model in the gas-phase. In solution these contributions will be considerably smaller leading to a systematic underestimation of the reaction free energy in the calculated dimerization free energies (see SI).[47,48] The driving force for the bond formation is the pairing of the two unpaired electrons in the monomer which overcompensates the Coulombic repulsion. Of course, the polar medium (HFIP) plays a central role in this regard as it screens the two charges enough to allow for the bond formation while in the gas phase the dimerization is unfavorable. As expected, the effect of the solvent is dominated by indirect interactions, i.e. the relatively high permittivity of the bulk phase which is modeled by a polarizable continu-

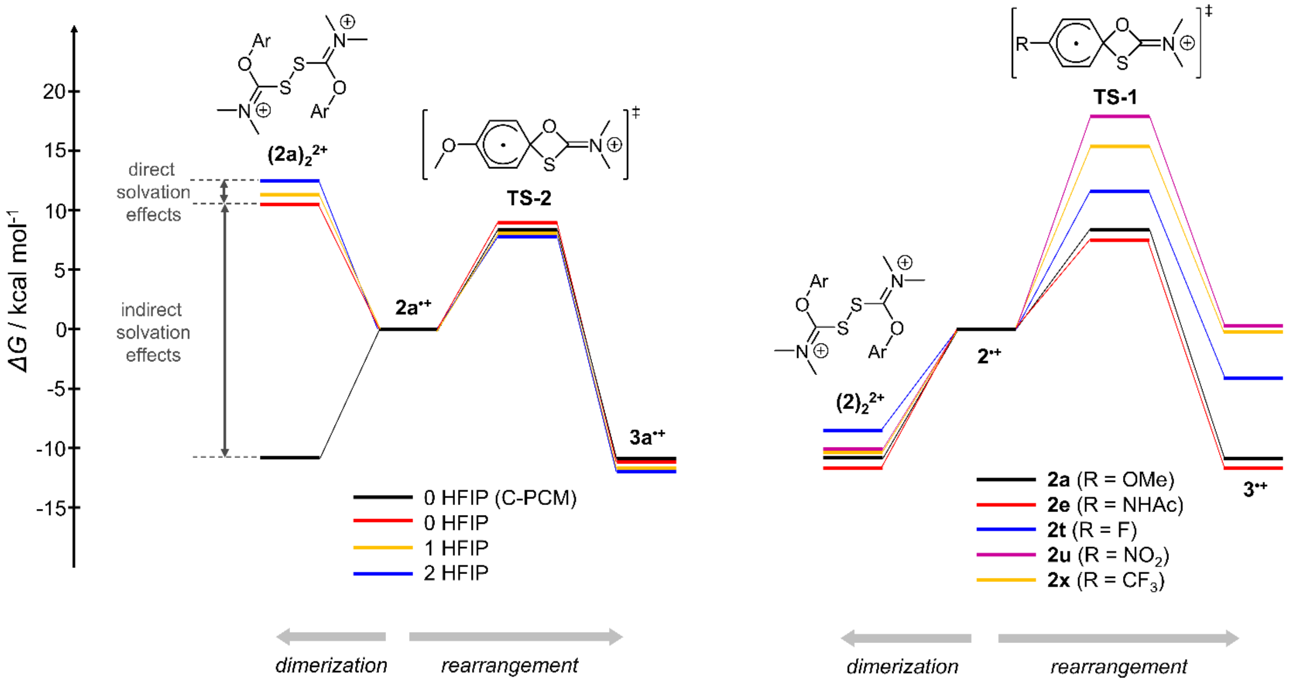

Figure 6. Left: Calculated free energy profile for the formation of **(2a)**$_2^{2+}$ versus the rearrangement towards **3a**$^{\bullet+}$ using different solvation models. While solvation has only a limited effect on the barrier and free reaction energy of the rearrangement it is integral for the dimerization. Right: Calculated free energy profiles for the formation of **(2)**$_2^{2+}$ versus the rearrangement towards **3**$^{\bullet+}$ for multiple *para*-substituted derivatives. Thiocarbamates featuring electron-withdrawing groups are subject to higher reaction barriers and lower reaction free energies than derivatives with electron-donating groups.

Table 2. Calculated free energies and reaction barriers in kcal mol^{-1} for selected conversions 2→3 (implicit solvation, for details see the experimental section).

Structure	Compound	Yield 3 [%]^a	$\Delta G(3/2)$	$\Delta G(3^{\bullet+}/2^{\bullet+})$	$\Delta G^{\ddagger}$	$\Delta G((2)_2^{2+}/2^{\bullet+})$
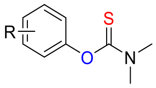	**2a** (R = 4-OMe)	95 (>99)^b	-12.8	-10.9	8.4	-10.8
	2e (R = 4-NHAc)	71	-12.6	-11.1	7.5	-11.7
	2t (R = 4-F)	n. d.	-11.9	-4.1	11.6	-8.5
	2u (R = 4-NO$_2$)	n. d.	-11.8	0.3	17.9	-10.1
	2x (R = 4-CF$_3$)	n. d.	-11.9	-0.2	15.4	-9.9
	2h (R = 2-OMe)	93	-12.3	-13.0	4.1	-17.8
	2y (R = 3-OMe)	n. d.	-12.0	-6.2	14.7	-10.3

^{a} Isolated yields of the batch electrolyses taken from ref. 15. ^{b} Isolated yield under optimized flow conditions.

um in the quantum chemical calculations. As depicted in the left panel of Figure 6, the usage of such a continuum solvation model shifts the reaction free energy by about –20 kcal/mol while the explicit addition of solvent molecules that form strong hydrogen bonds to the substrate has only a minor effect.

The energy profiles for species **2e**, **2h**, **2t**, **2u** and **2x** shown in the right panel of Figure 6 illustrate the relevance of the aforementioned dimerization for the observed selectivity. For all species bearing electron-withdrawing groups (**2t**, **2x** and **2u**) the rearrangement product formation is less favorable by ~5-10 kcal mol^{-1} than the dimerization. In contrast, the rearrangement products **3a** and **3e** are isoenergetic to the corresponding dimer to within ~1-2 kcal mol^{-1}. Furthermore, the associated reaction barriers are consistently higher for **2t**, **2x** and **2u** as compared to **2a** and **2e** (~4-8 kcal mol^{-1} versus ~11-18 kcal mol^{-1}). The calculated reaction free energies and barriers for the 2-, 3-, and 4-methoxy substituted thiocarbamates **2a**, **2h** and **2y** follow the same trend and highlight the importance of the position of the activating substituent on the aromatic ring (see Table 2).

At this point, we would like to reiterate that even in the non-ENKR cases, the reaction barriers of the rearrangement alone are not high enough to prohibit the occurrence of the rearrangement at the given reaction conditions. Only the subtle interplay between the two reaction channels provides an explanation for the observed trend in reactivity consistent with all experimental evidence.

Comparison to the thermal NKR. Figure 7 shows a comparison between the computed Gibbs free energies of the thermal and electrochemical NKR using the **2a**/**3a** couple as an example. In good agreement with the literature,[45] our calculations indicate a concerted thermal process via spirocyclic **TS-1**. The computed activation barrier amounts to 48.9 kcal mol^{-1} and the Gibbs free energy to −12.8 kcal mol^{-1}. While the same ΔG value also represents the driving force for the electrochemical reaction, the ENKR proceeds via a second reaction channel opened by the anodic generation of $\mathbf{2}^{\bullet+}$. In this way, the substrate is elevated to an entirely new potential energy surface with considerably altered properties, e.g. reaction barriers. The required energy for the "electrochemical excitation" of **2a** corresponds to 148.7 kcal mol^{-1} according to our quantum chemical calculations. It should be noted that *i*) this substantial amount of energy is completely provided by the electrode potential (E vs. vacuum level) and *ii*) the actually required minimum energy to trigger the chain process corresponds to the equilibrium cell voltage, i. e. the difference between $E_0(\mathbf{2}/\mathbf{2}^{\bullet+})$ and the potential required for proton reduction on platinum (which is the cathodic half-cell reaction in our system).

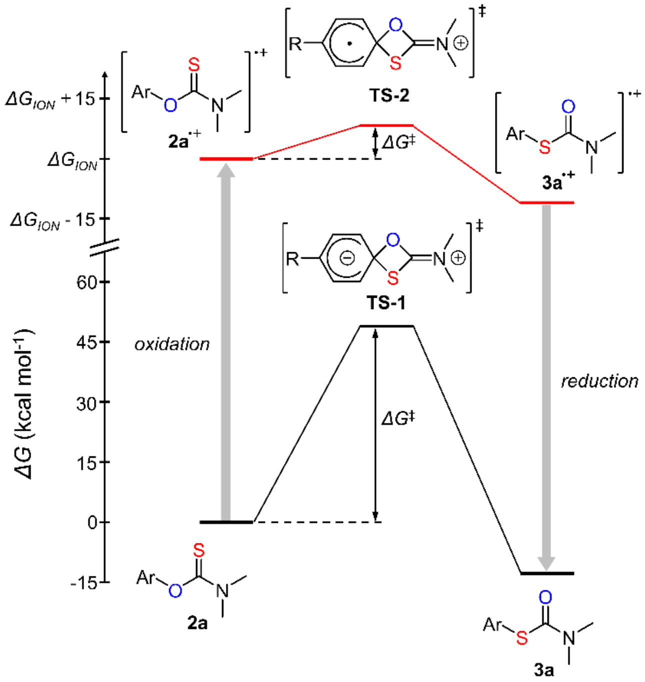

Figure 7. Comparison between the energy profiles of the thermal and the electrochemical NKR. ΔG values obtained from quantum chemical calculations in kcal mol^{-1}. All values were obtained from the combination of DLPNO-CCSD(T)/CBS for electronic energies and ωB97X-D3/def2-TZVP(-f) with C-PCM for thermochemical corrections and solvation energies, respectively (see the experimental section for further details).

Compared to the thermal process $\mathbf{2} \rightarrow \mathbf{3}$, the calculated barrier for $\mathbf{2}^{\bullet+} \rightarrow \mathbf{3}^{\bullet+}$ via **TS-2** is much lower (8.4 kcal mol^{-1}), whereby the rearrangement becomes slightly less exergonic (ΔG = −10.9 kcal mol^{-1}). The low activation barrier allows the cation radical rearrangement to proceed at room temperature, whereas the decreased Gibbs free energy of the cation radical rearrangement explains why the chain process proceeds spontaneously. After all, it is precisely the difference between $\Delta G(\mathbf{2a}/\mathbf{3a})$ and $\Delta G(\mathbf{2a}^{\bullet+}/\mathbf{3a}^{\bullet+})$ that represents the driving force for the chain propagation (and BET from the electrode at a given potential, respectively). Finally, this leads to a possible explanation for the positive influence of HFIP on the reaction. The fluorinated alcohol is known as a strong H-bond donor and among the four species $\mathbf{2a}^{\bullet+}$, **2a**, **3a** and $\mathbf{3a}^{\bullet+}$, compound **3a** is the one that is best stabilized via the carbonyl group as H-bond acceptor. Our calculations with explicit solvent molecules (see Table 3) support this assessment.

Table 3. Calculated influence of explicit solvation on the reaction free energies of $\mathbf{2a}^{\bullet+} \rightarrow \mathbf{3a}^{\bullet+}$ and $\mathbf{2} \rightarrow \mathbf{3}$ (for details see the experimental section).

number of explicit HFIP molecules	$\Delta G(3a^{\bullet+}/2a^{\bullet+})$ [kcal mol^{-1}]	$\Delta G(3a/2a)$ [kcal mol^{-1}]
0	10.9	11.6
1	12.0	13.6
2	11.7	14.8

Comparison to photoredox catalysis. The presented case illustrates the functional principle of electrochemical catalysis in a very clear way and furthermore, reveals strong parallels to photoredox catalyzed redox-neutral reactions. In the latter scenario, the injected light energy leads to excitation of a photosensitizer $\mathbf{PS}^{n+}$, which then abstracts an electron from the substrate to generate a reactive species $\mathbf{A}^{\bullet+}$ (see Scheme 3). After conversion to $\mathbf{P}^{\bullet+}$, the intermediate is either reduced by **A** in a chain propagation step or by $\mathbf{PS}^{(n-1)+}$, thus forming a closed catalytic cycle. For a number of photoredox-catalyzed transformations such as cation radical Diels-Alder reactions or anion radical [2+2] cycloadditions, the co-existence of chain processes and catalytic loops was indeed demonstrated.[49] In the proposed analogy, these closed photocatalytic loops correspond to the ECE^{b} mechanism in electrochemical catalysis.

SCHEME 3. Schematic illustration of the parallels between photoredox catalysis and electrochemical catalysis.

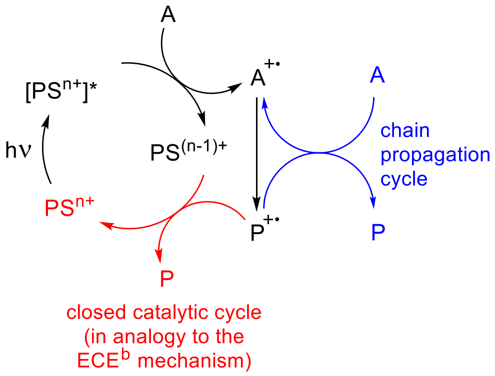

At this point we would like to highlight the similarities between the quantum yield Φ (number of conversions per injected photon) and TON_e (number of conversions per transferred electron),[8] both metrics being increased by the chain propagation cycle. However, a major difference is that the BET between ground state $\mathbf{PS}^{(n-1)+}$ and $\mathbf{P}^{\bullet+}$ leads to the waste of a photon (thus lowering Φ). Moreover, the unproductive

BET between $\mathbf{PS}^{(n-1)+}$ and $\mathbf{A}^{\bullet+}$ (leading to **A** and ground state $\mathbf{PS}^{n+}$) is usually exergonic and further decreases the efficiency of the photochemical process.[50] In contrast, such an unproductive step is completely suppressed in electrochemical catalysis. The BET as a part of the ECE^{b} mechanism does not have any negative impact on TON_e, which can be ascribed to the electrode remaining in the "excited state" after the initial electron transfer and consequently, TON_e values of up to 15 were achieved for the ENKR of **2a**.[15]

Another parallel becomes apparent when comparing the excitation steps. In each case, external energy input is required for the excitation step, albeit its source differs. While in photoredox catalysis, the energy input is defined by the wavelength of the incident light, the equilibrium cell voltage ΔE_0 (difference between $E_0(\mathbf{A}/\mathbf{A}^{\bullet+})$ and E_0 of the cathodic half-cell reaction) can be considered as the electrochemical counterpart. Of course, ΔE_0 accounts only for the required minimum amount of energy, since additional barriers have to be overcome to achieve current flow (e. g. kinetic inhibitions and the Ohmic resistance of the cell).

The differences and similarities between electrochemical catalysis and photoredox catalysis are well illustrated by a comparison between the ENKR and the photochemical NKR (PNKR) reported by Nicewicz et al. The PNKR was proposed to proceed via the pathways shown in Scheme 3, whereby **PS** corresponds to a pyrylium catalyst and **A**/**P** to **2**/**3**.[46] The photoexcitation was achieved by using blue LEDs (450 nm). This corresponds to an excitation energy of 63.5 kcal mol^{-1}, which is considerably above the minimum energy required for triggering electrochemical catalysis. The latter value amounts to 37.7 kcal mol^{-1} and is calculated from the difference between $E_{P/2}(\mathbf{2}/\mathbf{2}^{\bullet+})$ (1.63 V vs. SHE) and E_0 for proton reduction (approximated by SHE). While this consideration is rather theoretical, there is also a more tangible parallel with practical consequences: In both the ENKR and the PNKR, an off-cycle dimerization has been proposed (in our case leading to $(\mathbf{2})_2^{2+}$ as described above). However, the impact on the efficiency of the desired rearrangement is fundamentally different. In the PNKR case, a negative influence on quantum yield and reaction rate were described, which was explained by the unproductive BET between the dimer and the reduced ground state of the photocatalyst (Scheme 4, top).

SCHEME 4. Comparison between the impact of the off-cycle dimerization equilibrium on the photocatalytic and the electrochemically catalyzed process.

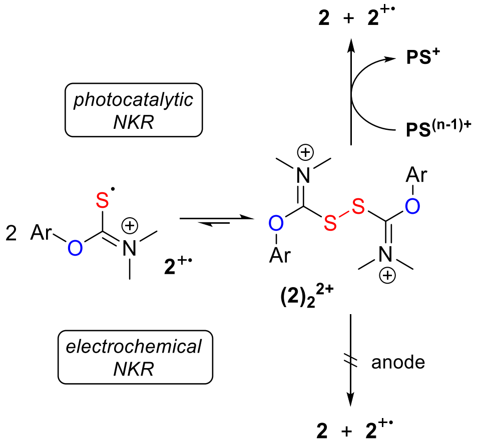

This was evidenced by monitoring the conversion at different initial concentrations (c_0) of **2a**, whereby an increase from 0.06 M to 0.25 M led to a 55% decrease in Φ and to a 15-fold increase of the time required for 95% conversion. As pointed out above, such an unproductive reduction of $(\mathbf{2a})_2^{2+}$ should not be possible in the NKR case due to the electrode residing in the "excited state" after the initial electron transfer. In order to probe this hypothesis, we carried out controlled current electrolyses at different initial concentrations (c_0) of **2a** and monitored the conversion with GC-FID (see Figure 8). Indeed, the normalized concentration profile of **3a** (fractional yield) shows no significant influence of c_0(**2a**). The absence of the discussed unproductive pathway can thus be considered as an advantage of the electrochemical method.

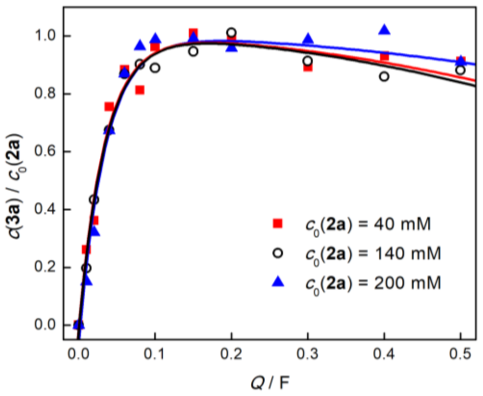

Figure 8. Fractional yields of **3a** during the electrolysis of **2a** (for details see the SI). The concentrations were determined via GC-FID using an internal standard.

The unusual behavior of dimethylaniline derivative 2p. The Hammett plot in Figure 3 clearly shows that **2p**/**3p** with R = 4-NMe$_2$ assumes a special role among the investigated reaction couples. While our previous synthetic study demonstrated that **2p**→**3p** is feasible under standard electrolysis conditions (35% isolated yield after passing 1.3 F),[15] the voltammetric responses are rather unusual. Both **2p** and **3p** exhibit a well-behaved reversible redox couple centered around 0.78 V (see Figure 9), which is significantly below the potentials predicted by eq. 5 and 6, respectively.

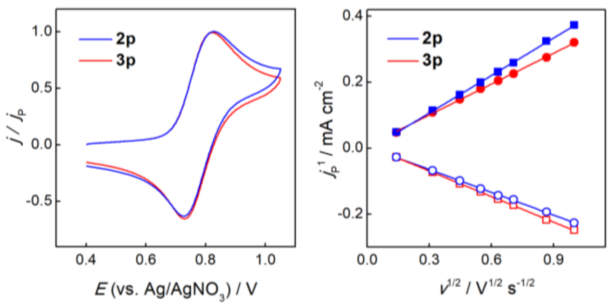

Figure 9. Left: Normalized current responses **2p** and **3p** recorded at 100 mV s^{-1} and 1 mM **2p** (**3p**). Right: Plot of the peak current densities vs. $v^{1/2}$.

On the voltammetry timescale, **2p**/**2p**$^{•+}$ and **3p**/**3p**$^{•+}$ are the only chemically reversible redox couples within the entire series **2** and **3**. We attribute these findings to a relocation of charge and spin density from the thiocarbamate unit to the amino group and the aryl ring consistent with the computed spin density for **2p**$^{•+}$ (see Figure 10). The observed chemical reversibility is in good agreement with other cases involving the oxidation of 4-substituted arylamines reported in the literature.[51-53]

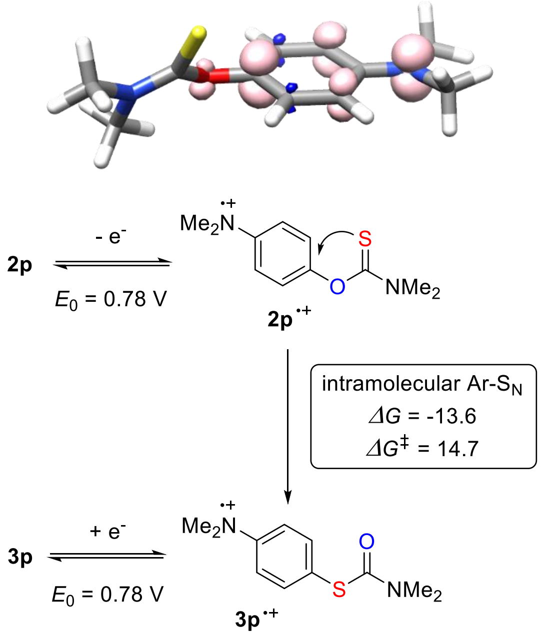

Figure 10. Top: Isosurface of the calculated spin density of **2p**$^{•+}$ at a value of 0.01 electron spins. Bottom: Mechanistic consequence for the rearrangement **2p**→**3p**. ΔG values obtained from quantum chemical calculations (kcal mol^{-1}, for details see the experimental section).

The relocation of charge and spin density has a significant impact on the reaction mechanism. First, the anodic oxidation serves the activation of the aromatic ring and not of the thiocarbamate unit. The **2p**$^{•+}$→**3p**$^{•+}$ rearrangement thus corresponds to an intramolecular ArS$_N$ (in analogy to the thermal NKR), which is supported by a negative computed Gibbs free energy (−13.6 kcal mol^{-1}) and a relatively low activation barrier (14.7 kcal mol^{-1}.). Second, since the potential of the **2p**/**2p**$^{•+}$ couple is the same as for **3p**/**3p**$^{•+}$, there is insufficient driving force for an efficient chain process.

To interrogate the proposed intermolecular ArS$_N$-type mechanism and to exclude alternative pathways via possible twofold oxidized intermediates, we have carried out a controlled potential electrolysis at 0.80 V (20 mV more positive than E_0(**2p**/**2p**$^{•+}$)). A divided cell was used in order to avoid discharge of radical cation intermediates at the cathode. The experiment showed that the ENKR indeed proceeds at the potential of the **2p**/**2p**$^{•+}$ couple, thus ruling out alternative pathways. The yield in **3p** was monitored via GC-FID (internal standard, see Table 4 and the SI). Interestingly, over-stoichiometric quantities of **3p** are initially formed with respect to the consumed charge. After passing 0.25 F, the turnover number per transferred electron (TON_e) amounted to 2.1. However, this TON_e is more than one order of magnitude below the initial TON_e determined for **2a**,[15] underlining the lack of driving force for the chain process due to E_0(**2p**/**2p**$^{•+}$) being equal to E_0(**3p**/**3p**$^{•+}$). Furthermore, a maximum yield of 77% in **3p** was obtained at 0.75 F. Upon further charge consumption, the yield gradually drops due to formation of an unidentified side product, which shows that a careful optimization of the charge equivalents is crucial for this special case.

Table 4. Controlled potential electrolysis of compound 2p.

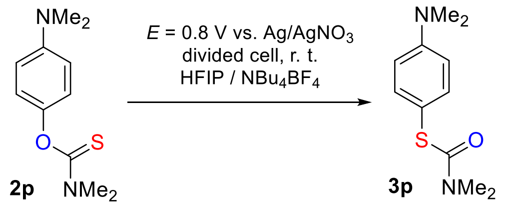

Q mol^{-1} [F]	3p [%]^a	TON_e
0.25	53	2.1
0.5	66	1.3
0.75	77	1.0
0.9	70	0.8
1.0	64	0.6

^{a} Determined GC-FID using an internal standard.

Electrolysis of *S*-arylthiocarbamate 3a. Investigating the behavior of the rearranged products **3** under electrolysis conditions is useful for understanding the ENKR in two respects: First, characterization of the products would explain the chemical irreversibility of the **3**/**3**$^{•+}$ couple in the CVs, including the unusual line crossing between the forward and the backward scan (see Figure 1 and Figure 3). Second, the experiment would reveal side reactions that may occur during electrolysis when more charge is applied than required for complete conversion (see also the slow decay of c(**3**) between 0.3 and 0.5 F in Figure 8). Therefore, we have electrolyzed **3a** as a representative of the ENKR-susceptible **2**/**3** couples with a stoichiometric amount of charge for the analysis of the products (see Scheme 5).

SCHEME 5. Electrolysis of 3a including the anodic peak potentials of products 6a and 7a.

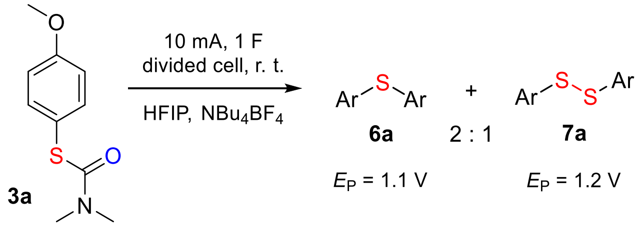

To avoid possible reduction of intermediates at the cathode, we have used a divided cell for the experiment. After passing 1 F, a 2:1 mixture of diaryl sulfide **6a** and diaryl disulfide **7a** was formed, while **3a** was almost entirely consumed. Aside from the identification of overoxidation products, this discovery may lead to the development of a useful two-step one-pot electrolysis, where **4** or **5** are directly generated from **2** (provided that the selectivity can be controlled in either direction).

Compounds **6a** and **7a** were isolated and subjected to CV analysis (Figure S11). The estimated peak potentials ($E_P(\mathbf{6a})$ = 1.1 V, $E_P(\mathbf{7a})$ = 1.2 V) explain the line crossing in the CVs of **3a**. Thus, **6a** and **7a** are easier to oxidize than **3a**, which leads to additional anodic contributions after reversal of the scan direction. Knowing the fate of $\mathbf{3}^{\bullet+}$ at elevated potentials and with eqs. 1-4 and as well as the off-cycle dimer $(\mathbf{2a})_2^{2+}$ (eq. 8) in mind, it is possible to obtain an accurate fit between the digital simulation of the extended kinetic model and the full CV of **2a** (Figure 11, for details see the SI).

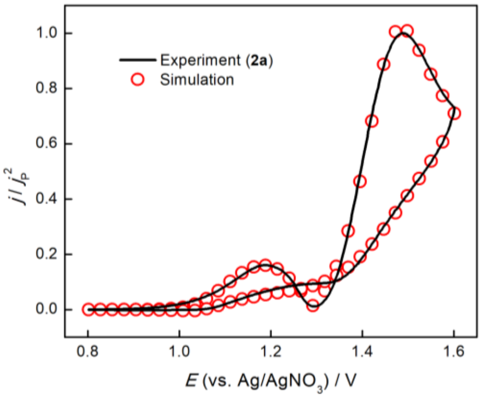

Figure 11. Digital simulation (red circles) of the normalized CV of 5 mM **5a** (solid line, v = 400 mV s^{-1}) using eqs. 1-4 and taking into account the off-cycle dimer $(\mathbf{2a})_2^{2+}$ as well as the formation of **6a** and **7a** (Scheme 5). The simulations were carried out using the DigiElch package.[40]

At this point, it should be highlighted that the formation of **6a** and **7a** can only be initiated when species **2a** is depleted. Using the standard electrolysis protocol,[15] this side-reaction is usually not observed, which can be explained in two ways: First, in a galvanic electrolysis the anode potential is close to $E^1_{P/2}(\mathbf{2a})$ as long as sufficient **2a** is available for oxidation. At this potential, $\mathbf{3a}^{\bullet+}$ is reduced to **3a** by means of BET (ECE^b mechanism). Second, $\mathbf{3a}^{\bullet+}$ is "protected" in the presence of **2a** by reaction through the thermodynamically favorable chain process.

On the use of alternative solvents. As discussed before,[15] HFIP offers a number of advantages with respect to the ENKR such as excellent electrochemical properties, low nucleophilicity and good hydrogen bonding strength.[54,55] A further interesting feature is that due to the relatively low boiling point (58 °C), the solvent can be conveniently recovered and recycled. However, the initial cost (currently ~99£/kg, Fluorochem Ltd.) is certainly a drawback and we have therefore tested alternative solvents during the optimization of our procedure.[15] We found that the use of MeOH, CH_2Cl_2, and CH_3CN under standard electrolysis conditions does not lead to the formation of **3**, whereas ENKR is possible in 2,2,2-trifluoroethanol (albeit in significantly lower yields).

Two recent studies showed that the cation radical NKR triggered by chemical oxidants can be carried out in DMSO at room temperature and in CH_3CN/H_2O (3:1) at temperatures in the range of 45 - 65 °C.[27,28] We were therefore interested in whether the ENKR is possible in these solvents and tested **2a** under standard electrolysis conditions (general procedure II, for details see the SI). No conversion was achieved in DMSO even after passing 1 F, whereas electrolysis in CH_3CN/H_2O (3:1) rendered small amounts of **3a** along with an unidentified byproduct. While in the latter case, optimization of the electrolysis conditions may lead to improved results in the future, HFIP currently remains the solvent of choice for the ENKR.

▪ Conclusion

Through a combination of experimental and quantum chemical methods we have obtained mechanistic key-information on the electrochemically catalyzed Newman-Kwart rearrangement. Analogously to other routes mediated by chemical oxidants, a sequence proceeding via cation radical intermediates was identified as the most likely mechanism. Both the experimental data and the calculations indicate that with the exception of the 4-NMe_2-substituted *O*-phenylthiocarbamate, charge and spin density are predominantly located on the thiocarbamoyl unit, and that consequently, the cation radical rearrangement can be considered as an intramolecular Ar-S_E reaction.

The unusual voltammetric profile of the *O*-aryl thiocarbamates was deciphered by varying scan rate and concentration, isolation of electrolysis products as well as digital simulations. Through the evaluation of the CVs of 25 reaction couples, diagnostic criteria for the prediction of the feasibility for specific substrates were derived. We expect that in the future, this analytical approach will be useful for the development of further electrochemically catalyzed redox-neutral reactions.

Our quantum chemical calculations have shown that the activation barrier alone cannot sufficiently explain the susceptibility of specific substrates toward the ENKR. It is much rather the interplay between the kinetic inhibition of the rearrangement and the thermodynamically favorable equilibrium formation of an off-cycle dimer that determines the feasibility for specific substrates. Concentration and temperature are therefore parameters that could help to extend the scope of the ENKR to less activated arenes, albeit at the expense of productivity and energy efficiency.

Furthermore, the benign influence of the solvent HFIP was explained by inclusion of explicit solvent molecules into the calculations. The resulting H-bond interactions both decrease the activation barrier of the rearrangement and improve the thermodynamics of the final reduction step, thereby adding driving force to the chain mechanism.

The comparison between photochemically and electrochemically induced NKR shows several parallels, such as the mode of excitation and the co-existence of the chain mechanism and the back-electron transfer. On the other hand, a significant difference is that in electrochemical catalysis the BET does not lead to a decrease of the efficiency of the process. This is due to the fact that the electrode remains in the "excited state" after oxidation, whereas in photoredox catalysis BET proceeds between the reactive intermediate and the ground state of the catalyst. A practical consequence is that in the photochemical NKR, an increase in concentration leads to a lower efficiency of the reaction, whereas no significant concentration effect was observed for the ENKR. We believe that these insights will contribute to cross-fertilization between electrosynthesis and photoredox catalysis and will be of great benefit for the development of further electrochemically catalyzed processes.

▪ Experimental section

General information. Most of the *O*-arylthiocarbamates **2** and their *S*-aryl derivatives **3** were synthesized according to our previously described procedures.[15] The syntheses of the examples which are not part of ref. 15 are described below. ^{1}H, ^{13}C and ^{19}F NMR spectra were recorded using an AVANCE 250, 300 or 500 spectrometer (Bruker). Chemical shifts are reported in parts per million (ppm, δ scale) and referenced to the signal of residual non- or partially deuterated solvent. Mass spectrometry (MS) was carried out either with electron ionization (EI) or with electrospray ionization (ESI) using a MAT 95 XP (Thermo Finnigan). GC-FID was carried out using a HP 1100 (Thermo Fisher) equipped with a 30 m HP-5 column. All dry solvents were purchased from Acros Organics (AcroSeal) and used as received, if not stated otherwise. Tetrabutylammonium perchlorate and tetrafluoroborate were purchased from Sigma Aldrich (both electrochemical grade) and used as received. 1,1,1,3,3,3-Hexafluoroisopropanol (HFIP, >99% purity) was purchased from Fluorochem and used as received. The glassy carbon electrodes (Sigradur® K) were purchased from HTW GmbH (Tierhaupten, Germany) and the reticulated vitreous carbon electrodes (RVC 3000C, ρ = 0.05 g cm^{-3}, porosity = 96.5%) from Goodfellow Ltd. (Cambridge, England).

General procedure I (cyclic voltammetry). The experiments were carried out in a custom-made three-electrode cell using a PGSTAT 128N (Autolab). A glassy carbon disk (diameter: 1.6 mm) served as the working electrode and a platinum wire as the counter electrode. The glassy carbon disk was polished using polishing alumina (0.05 µm) prior to each experiment. As reference, a Ag/AgNO$_3$ electrode (silver wire in 0.1 MNBu$_4$BF$_4$/CH$_3$CN solution; c(AgNO$_3$) = 0.01 M; E_0 = −87 mV vs. ferrocene/ferrocenium couple)[56] was used, and this compartment was separated from the rest of the cell with a Vycor frit. NBu$_4$BF$_4$ (0.1 M, electrochemical grade) was employed as supporting electrolyte in 1,1,1,3,3,3-hexafluoroisopropanol solution. The electrolyte was purged with Ar for at least 5 min prior to recording. Compounds **2** and **3**, respectively, were analyzed at a concentration of 1 mM and a scan rate of 100 mV s^{-1}, if not stated otherwise. The half-wave potentials ($E_{1/2}$) were extracted from background corrected voltammograms.

General procedure II (electrolysis in undivided cell). The experiments were carried out in a gastight undivided cell equipped with a RVC anode (height: 50 mm, depth: 5 mm, width: 10 mm) and a platinum wire (0.4 mm diameter) serving as the cathode. Both electrodes had an immersion depth of 10 mm. A solution of *N*,*N*-dimethylthiocarbamate (**2** or **3**, 1.0 mmol) and tetrabutylammonium tetrafluoroborate (1.0 mmol) in 10 mL HFIP was placed in the cell, purged with argon for five minutes and electrolyzed under stirring (700 rpm) at a constant current of 10 mA until an appropriate amount of charge was passed (reaction monitoring via TLC, GC-FID or GC-MS).

General procedure III (electrolysis in divided cell). The experiments were carried out in a gastight H-type divided cell equipped with a porous glass frit (G4) as a separator. A piece of reticulated vitreous carbon (height: 50 mm, depth: 5 mm, width: 10 mm) was used as a working electrode and a platinum plate (width: 10 mm) as a counter electrode. Both electrodes had an immersion depth of 10 mm. *N*,*N*-Dimethylthiocarbamates (**2** or **3**, 0.7 mmol), *para*-difluorobenzene (internal standard, 0.7 mmol) and tetrabutylammonium tetrafluoroborate (0.7 mmol) were dissolved in 7 mL HFIP and placed in the anodic half-cell. The cathodic half-cell was charged with a solution of tetrabutylammonium tetrafluoroborate (0.7 mmol) in 7 mL HFIP. Both solutions were purged with argon for five minutes prior to the experiment. The electrolysis was performed under stirring and a constant current of 10 mA.

Computational studies. The computational results were obtained from electronic structure calculations on multiple levels of theory. Here we first describe the computational details of all calculations that correspond to the gas-phase or apply implicit solvation models before introducing the approach to account for explicit solvent-solute interactions.

The ORCA program package in its version 4 was used throughout the former set of calculations.[57] All geometry optimizations were carried out at the DFT level using the ωB97X-D3 together with the def2-TZVP(-f) basis set.[58-60] In cases where solvation is taken into account it is modeled by a polarizable continuum model (C-PCM) with ε = 17.8 for HFIP.[61,62] All special points on the potential energy surface were verified by analyzing the corresponding Hessian matrix: Minima give rise to a positive definite Hessian matrix while the Hessian matrix of transition states feature a single negative eigenvalue. Refined electronic energies were obtained for gas-phase geometries using the DLPNO-CCSD(T) method that yields excellent approximations to the "gold standard of quantum chemistry" for closed-shell molecules, canonical CCSD(T).[63-66] The DLPNO-CCSD(T) energies were extrapolated to the complete basis set limit (CBS) by means of a two-point extrapolation scheme on the basis of energies calculated with the cc-PVTZ and cc-PVQC basis sets.[67-72] Thermochemical corrections to the coupled cluster electronic energy were estimated from the particle in a box, rigid rotor and harmonic approximations utilizing DFT frequencies to get the final Gibbs free energies in the gas phase, i.e $G_{gas}(CC) = E_{gas}(CC) + [G_{gas}(DFT) - E_{gas}(DFT)]$. In the solvent phase, the free energy difference between implicit solvation and gas phase calculations was added to the gas phase coupled cluster Gibbs free energy to get the final Gibbs free energy in the solvent phase, $G_{solvent}(CC) = G_{gas}(CC) + [G_{solvent}(DFT) - G_{gas}(DFT)]$. During all aforementioned calculations the resolution of identity (RIJ) in combination with the def2/J basis set and chain-of-spheres (COSX) approximations were used to accelerate the evaluation of two-electron integrals.[73-77]

Explicitly solvated geometries with 1 and 2 HFIP molecules were obtained in the following steps: 1) 300 geometries were sampled using the ABCluster 2.0 program[78,79] tailored with the xTB6.1 program for the energies.[80] 2) The 10 structures lowest in energy in the previous step were sampled further with the crest program.[81] 3) The lowest energy structure for each case was then taken for optimization at DFT-GGA level with the B97-3c functional.[82] 4) The subsequent hybrid-DFT geometry optimizations and electronic energy refinements were performed as described above.

General procedure IV (synthesis of thiocarbamates). A modified version of a previously described procedure was used to synthesize the target compounds.[15] For the synthesis of compound **2**, the corresponding phenol **1** (1.00 g) was dissolved in 10 mL dry DMF in an argon flushed, dry Schlenk flask. The solution was cooled to 0 °C followed by addition of 1.1 equiv. sodium hydride (60 wt% in mineral oil) in small portions, whereby the temperature was kept between 0 °C and 5 °C. After stirring the mixture for 30 min at 0 °C, 1.3 equiv. *N*,*N*-dimethyl thiocarbamoyl chloride were added in a single portion. The reaction mixture was allowed to warm up to room temperature and then poured into ca. 50 mL water, which led to precipitation of the crude product. After storing the mixture overnight at 0 °C, the precipitate was filtered off and recrystallized from boiling *n*-heptane or *n*-heptane/ethyl acetate. For the synthesis of compound **3** the same procedure was applied, whereby thiophenols (**4**) were used as starting material instead of **1**.

***O*-Phenyl-*N*,*N*-dimethylthiocarbamate (2s).** Phenol (1.42 g, 15.06 mmol), *N*,*N*-dimethylthiocarbamoyl chloride (2.440 g, 19.74 mmol) and sodium hydride (0.663 g, 60 wt% in mineral oil, 16.58 mmol) were reacted in 14 mL DMF according to general procedure IV. The addition of 70 mL water to the reaction mixture led to precipitation of the crude product as a viscous yellow oil, which was purified using column chromatography (*n*-heptane/ethyl acetate 6:1). After recrystallization from *n*-heptane, **2s** was obtained as a colorless solid. The analytical data are in agreement with the literature.[83] Yield: 1.694 g (9.34 mmol, 62%). M. p.: 31.0 – 32.0 °C (lit.: 29.5 – 30.5 °C).[83] ^{1}H NMR (250 MHz, chloroform-*d*): δ(ppm) = 3.38 (s, 3H), 3.49 (s, 3H), 7.04 - 7.17 (m, 2H), 7.23 - 7.34 (m, 1H), 7.37 - 7.52 (m, 2H). ^{13}C{^{1}H} NMR (63 MHz, chloroform-*d*): δ(ppm) = 38.6, 43.2, 122.7, 125.8, 129.1, 154.0, 187.8.

***O*-(4-Fluorophenyl)-*N*,*N*-dimethylthiocarbamate (2t).** 4-Fluorophenol (2.187 g, 19.42 mmol), *N*,*N*-dimethylthiocarbamoyl chloride (3.167 g, 25.62 mmol) and sodium hydride (0.856 g, 60 wt% in mineral oil, 21.40 mmol) were reacted in 22 mL DMF according to general procedure IV. The addition of 110 mL water to the reaction mixture led to precipitation of the crude product as a pale-yellow solid. After recrystallization from *n*-heptane, **2t** was obtained as an off-white solid. The analytical data are in agreement with the literature.[21] Yield: 3.246 g (16.29 mmol, 84%). M. p.: 75.5 – 77.5 °C (lit.: 75 – 77 °C).[21] ^{1}H NMR (300 MHz, chloroform-*d*): δ(ppm) = 3.35 (s, 3H), 3.46 (s, 3H), 6.98 - 7.13 (m, 4H). ^{13}C{^{1}H} NMR (63 MHz, chloroform-*d*): δ(ppm) = 38.6, 43.3, 115.7 (d, *J* = 23.3 Hz), 124.1 (d, *J* = 8.7 Hz), 149.8 (d, *J* = 2.7 Hz), 160.2 (d, *J* = 244.4 Hz), 187.7. ^{19}F NMR (282 MHz, chloroform-*d*): δ (ppm) = –116.8.

***O*-(4-Chlorophenyl)-*N*,*N*-dimethylthiocarbamate (2v).** 4-Chlorophenol (2.191 g, 17.04 mmol), *N*,*N*-dimethylthiocarbamoyl chloride (2.743 g, 22.19 mmol) and sodium hydride (0.755 g, 60 wt% in mineral oil, 18.88 mmol) were reacted in 22 mL DMF according to general procedure IV. The addition of 110 mL water to the reaction mixture led to precipitation of the crude product as a pale-yellow solid. After recrystallization from *n*-heptane, **2v** was obtained as an off-white solid. The analytical data are in agreement with the literature.[21] Yield: 2.616 g (12.13 mmol, 71%). M. p.: 52.5 – 54.5 °C (lit.: 51 – 52 °C).[21] ^{1}H NMR (250 MHz, chloroform-*d*): δ(ppm) = 3.34 (s, 3H), 3.45 (s, 3H), 6.95 - 7.08 (m, 2H), 7.30 - 7.41 (m, 2H). ^{13}C{^{1}H} NMR (63 MHz, chloroform-*d*): δ(ppm) = 38.7, 43.3, 124.1, 129.2, 131.3, 152.4, 187.4.

***O*-(4-Carbomethoxyphenyl)-*N*,*N*-dimethylthiocarbamate (2w).** 4-Carbomethoxyphenol (1.723 g, 11.32 mmol), *N*,*N*-dimethylthiocarbamoyl chloride (1.828 g, 14.79 mmol) and sodium hydride (0.501 g, 60 wt% in mineral oil, 12.53 mmol) were reacted in 17 mL DMF according to general procedure IV. The addition of 85 mL water to the reaction mixture led to precipitation of the crude product as a pale-yellow solid. After recrystallization from *n*-heptane/ethyl acetate, **2w** was obtained as a colorless solid. The analytical data are in agreement with the literature.[21] Yield: 1.708 g (7.14 mmol, 63%). M. p.: 92.5 – 95.0 °C (lit.: 94.5 – 95.5 °C).[21] ^{1}H NMR (250 MHz, chloroform-*d*): δ(ppm) = 3.36 (s, 3H), 3.46 (s, 3H), 3.91 (s, 3H), 7.09 - 7.19 (m, 2H), 8.03 - 8.14 (m, 2H). ^{13}C{^{1}H} NMR (63 MHz, chloroform-*d*): δ(ppm) = 38.8, 43.2, 52.1, 122.9, 127.7, 130.9, 157.4, 166.3, 186.9.

***O*-(4-Trifluorphenyl)-*N*,*N*-dimethylthiocarbamate (2x)**. 4-Trifluormethylphenol (0.784 g, 4.84 mmol), *N*,*N*-dimethylthiocarbamoyl chloride (0.755 g, 6.27 mmol) and sodium hydride (0.219 g, 60 wt% in mineral oil, 5.48 mmol) were reacted in 8 mL DMF according to general procedure IV. The addition of 40 mL water to the reaction mixture led to precipitation of the crude product as a pale-yellow solid. After recrystallization from *n*-heptane, **2x** was obtained as a colorless solid. The analytical data are in agreement with the literature.[21] Yield: 0.777 g (3.12 mmol, 64%). M. p.: 116 – 117.5 °C (lit.: 111 – 112 °C).[21] ^{1}H NMR (250 MHz, chloroform-*d*): δ(ppm) = 3.37 (s, 3H), 3.47 (s, 3H), 7.20 (d, *J* = 8.3 Hz, 2H), 7.67 (d, *J* = 8.3 Hz, 2H). ^{13}C{^{1}H} NMR (126 MHz, chloroform-*d*): δ(ppm) = 38.8, 43.2, 123.9 (q, *J* = 272.1 Hz), 126.43 (q, *J* = 3.7 Hz), 127.9 (q, *J* = 32.2 Hz), 156.3, 186.8. ^{19}F NMR (282 MHz, chloroform-*d*): *δ*(ppm) = –62.1.

***O*-(3-Methoxyphenyl)-*N*,*N*-dimethylthiocarbamate (2y).** 3-Methoxyphenol (0.89 mL, 8.1 mmol), *N*,*N*-dimethylcarbamoyl chloride (1.3 g, 10.5 mmol) and sodium hydride (0.35 g, 60wt% in mineral oil, 8.9 mmol) were reacted in 10 mL DMF according to general procedure IV. The reaction mixture was poured into water, followed by extraction with ethyl acetate. The organic layer was separated, dried over anhydrous sodium sulfate and evaporated under reduced pressure to give the crude product. Purification via column chromatography (toluene/ethyl acetate 40:1) gave **2y** as a yellow oil. The analytical data are in agreement with the literature.[21] Yield: 0.91 g (4.3 mmol, 54%). ^{1}H NMR (300 MHz, chloroform-*d*): *δ*(ppm) = 3.34 (s, 3H), 3.46 (s, 3H), 3.81 (s, 3H), 6.64 (dd, *J* = 2.3 2.3 Hz), 6.68 (ddd, *J* = 8.1, 2.3, 0.9 Hz, 1H), 6.81 (ddd, *J* = 8.3, 2.5, 0.8 Hz, 1H), 7.29 (dd, *J* = 8.1, 8.1 Hz, 1H). ^{13}C{^{1}H} NMR (63 MHz, chloroform-*d*): *δ*(ppm) = 38.7, 43.2, 55.4, 108.8, 111.7, 115.0, 129.4, 154.9, 160.3, 187.6.

***S*-(4-Methylphenyl)-*N*,*N*-dimethylthiocarbamate (3q).** 4-Methylthiophenol (0.999 g, 8.05 mmol), *N*,*N*-dimethylcarbamoyl chloride (1.0 mL, 10.9 mmol) and sodium hydride (0.354 g, 60 wt% in mineral oil, 8.85 mmol) were reacted in 10 mL DMF according to general procedure IV. The addition of 50 mL water to the reaction mixture led to precipitation of the crude product as a pale-yellow solid. After recrystallization from *n*-heptane, **3q** was obtained as a colorless crystalline solid. The analytical data are in agreement with the literature.[21] Yield: 0.331 g (1.70 mmol, 21%). M. p.: 36.5 – 38.0 °C (lit.: 37.0 – 39.5 °C).[21] ^{1}H NMR (250 MHz, chloroform-*d*): *δ*(ppm) = 2.38 (s, 3H), 3.06 (br. s., 6H), 7.15 - 7.25 (m, 2H), 7.34 - 7.44 (m, 2H). ^{13}C{^{1}H} NMR (63 MHz, chloroform-*d*): *δ*(ppm) = 21.2, 36.8, 125.2, 129.7, 135.6, 139.3, 167.2.

***S*-Phenyl-*N*,*N*-dimethylthiocarbamate (3s).** Thiophenol (1.446 g, 13.12 mmol), *N*,*N*-dimethylcarbamoyl chloride (1.575 mL, 17.14 mmol) and sodium hydride (0.578 g, 60 wt% in mineral oil, 14.45 mmol) were reacted in 14 mL DMF according to general procedure IV. The addition of 70 mL water to the reaction mixture led to precipitation of **3s** as a colorless solid without further purification. The analytical data are in agreement with the literature.[83] Yield: 1.414 g (7.80 mmol, 59%). M. p.: 43.0 – 46.0 °C (lit.: 43 – 44 °C).[83] ^{1}H NMR (300 MHz, chloroform-*d*): *δ*(ppm) = 3.07 (br. s., 6H), 7.35 - 7.44 (m, 3H), 7.47 - 7.55 (m, 2H). ^{13}C{^{1}H} NMR (63 MHz, chloroform-*d*): *δ*(ppm) = 36.8, 128.7, 128.8, 129.0, 135.6, 166.8.

***S*-(4-Nitrophenyl)-*N*,*N*-dimethylthiocarbamate (3u).** 4-Nitrothiophenol (1.014 g, 6.53 mmol), *N*,*N*-dimethylcarbamoyl chloride (0.8 mL, 8.7 mmol) and sodium hydride (0.288 g, 60 wt% in mineral oil, 7.20 mmol) were reacted in 10 mL DMF according to general procedure IV. The addition of 50 mL water to the reaction mixture led to precipitation of the crude product as a yellow solid. After recrystallization from *n*-heptane, **3u** was obtained as a pale-yellow solid. The analytical data are in agreement with the literature.[21] Yield: 0.826 g (3.65 mmol, 56%). M. p.: 119.0 – 122.0 °C (lit.: 117.5 – 119.5 °C).[21] ^{1}H NMR (250 MHz, chloroform-*d*): *δ*(ppm) = 3.09 (br. s., 6H), 7.68 (d, *J* = 8.8 Hz, 2H), 8.21 (d, *J* = 8.83 Hz, 2H). ^{13}C{^{1}H} NMR (63 MHz, chloroform-*d*): *δ*(ppm) = 37.0, 123.5, 135.5, 137.7, 147.9, 164.6.

***S*-(4-Chlorophenyl)-*N*,*N*-dimethylthiocarbamate (3v).** 4-Chlorothiophenol (1.309 g, 9.05 mmol), *N*,*N*-dimethylcarbamoyl chloride (1.08 mL, 11.80 mmol) and sodium hydride (0.399 g, 60 wt% in mineral oil, 9.98 mmol) were reacted in 13 mL DMF according to general procedure IV. After completed reaction, the mixture was transferred to a separation funnel, followed by addition of 65 mL water. After extraction with ethyl acetate (3 x 40 mL), the combined organic layers were washed with water (3 x 40 mL) and brine (25 mL). After evaporation of the solvent and recrystallization from *n*-heptane, **3v** was obtained as a colorless solid. The analytical data are in agreement with the literature.[21] Yield: 1.586 g (7.35 mmol, 81%). M. p: 78.0 – 80.5 °C (lit.: 74 – 76 °C).[21] ^{1}H NMR (300 MHz, chloroform-*d*): *δ*(ppm) = 3.06 (br. s., 6H), 7.33 - 7.39 (m, 2H), 7.39 - 7.46 (m, 2H). ^{13}C{^{1}H} NMR (63 MHz, chloroform-*d*): δ (ppm) = 36.9, 127.3, 129.1, 135.5, 136.9, 166.3.

***S*-(4-Carbomethoxyphenyl)-*N*,*N*-dimethylthiocarbamate (3w).** Step 1: Mercaptobenzoic acid (1.163 g, 7.54 mmol) was dissolved in methanol (30 mL) and three drops of sulfuric acid were added. The solution was stirred for 72 h, whereby the temperature was kept between 55 °C and the boiling point of the solution (monitoring of the conversion via ^{1}H NMR). After completed reaction, the solvent was removed under reduced pressure and the remaining solid dissolved in 15 mL ethyl acetate. The organic layer was washed with water (2 x 15 mL), saturated aq. $NaHCO_3$ (1 x 15 mL) and brine (1 x 15 mL). The solvent was removed under reduced pressure to give 0.861 g (5.12 mmol, 68%) of crude 4-mercaptobenzoic acid methylester. Step 2: The unpurified product of step 1 was converted with sodium hydride (0.226 g, 60 wt% in mineral oil, 5.65 mmol) and *N*,*N*-dimethylcarbamoyl chloride (0.615 mL, 6.69 mmol) in 9 mL DMF according to general procedure I. Precipitation with 45 mL water and recrystallization from *n*-heptane/ethyl acetate gave the product as an off-white solid. The analytical data are in agreement with the literature.[21] Yield: 0.769 g (3.21 mmol, 63%). MP.: 91.5 – 94.5 °C (lit.: 90 – 91 °C).[21] ^{1}H NMR (300 MHz, chloroform-*d*): *δ*(ppm) = 3.07 (br. s., 6H), 3.92 (s, 3H), 7.53 - 7.63 (m, 2H), 7.97 - 8.09 (m, 2H). ^{13}C{^{1}H} NMR (75 MHz, chloroform-*d*): *δ*(ppm) = 36.9, 52.2, 129.8, 130.4, 134.7, 134.9, 165.6, 166.5.

***S*-(4-Trifluorphenyl)-*N*,*N*-dimethylthiocarbamate (3x).** 4-Trifluoromethylthiophenol (1.095 g, 6.15 mmol), *N*,*N*-dimethylcarbamoyl chloride (0.735 mL, 8.01 mmol) and sodium hydride (0.272 g, 60 wt% in mineral oil, 6.80 mmol) were reacted in 11 mL DMF according to general procedure IV. The addition of 55 mL water to the reaction mixture led to precipitation of the crude product as a yellow solid. After recrystallization from *n*-heptane/ethyl acetate, **3x** was obtained as a colorless solid. The analytical data are in agreement with the literature.[21] Yield: 0.960 g (3.85 mmol, 63%). M. p.: 42.0 – 44.0 °C (lit.: 43 – 44 °C).[21] ^{1}H NMR (300 MHz, chloroform-*d*): *δ*(ppm) = 3.08 (br. s., 6H), 7.63 (br. s., 4H). ^{13}C{^{1}H} NMR (75 MHz, chloroform-*d*):

δ(ppm) = 36.9, 123.9 (q, J = 271.9 Hz), 125.6 (q, J = 3.7 Hz), 125.6 (q, J = 3.9 Hz), 131.0 (q, J = 32.5 Hz), 133.6, 135.6, 165.6. ^{19}F NMR (282 MHz, chloroform-d): δ(ppm) = –62.8.

***O*-(4-Fluorophenyl)-*N*,*N*-dimethylcarbamate (5t).** 4-Fluorophenol (1.89 g, 16.86 mmol), *N*,*N*-dimethylcarbamoyl chloride (2.440 mL, 21.99 mmol) and sodium hydride (0.749 g, 60 wt% in mineral oil, 18.73 mmol) were reacted in 18 mL DMF according to general procedure IV. Water (90 mL) was added and the mixture extracted three times with 50 mL ethyl acetate. The combined organic layers were washed with water (3 x 50 mL), with 25 mL brine and dried over sodium sulfate. After evaporation of the solvent, **5t** remained as a light-yellow oil. The analytical data are in agreement with the literature.[84] Yield: 2.802 g (15.30 mmol, 91%). ^{1}H NMR (500 MHz, chloroform-d): δ(ppm) = 3.01 (s, 3H), 3.10 (s, 3H), 6.93 - 7.17 (m, 4H). ^{13}C{^{1}H} NMR (75 MHz, chloroform-d): δ(ppm) = 36.4, 36.7, 115.7 (d, J = 23.7 Hz), 123.1 (d, J = 8.2 Hz), 147.4 (d, J = 2.7 Hz), 154.82, 159.87 (d, J = 243.2 Hz). ^{19}F NMR (282 MHz, chloroform-d): δ (ppm) = –118.2.

***O*-(4-Chlorophenyl)-*N*,*N*-dimethylcarbamate (5v).** 4-Chlorophenol (1.92 g, 14.93 mmol), *N*,*N*-dimethylcarbamoyl chloride (1.785 mL, 19.39 mmol) and sodium hydride (0.656 g, 60 wt% in mineral oil, 16.40 mmol) were reacted in 19 mL DMF according to general procedure IV. After addition of 95 mL water, the was extracted three times with 50 mL ethyl acetate. The combined organic layers were washed with water (3 x 50 mL), with 25 mL brine and dried over sodium sulfate. After evaporation of the solvent, **5v** remained as a colorless oil. The analytical data are in agreement with the literature.[85] Yield: 2.516 g (12.60 mmol, 84%). ^{1}H NMR (500 MHz, chloroform-d): δ(ppm) = 3.01 (s, 3H), 3.09 (s, 3H), 7.07 (d, J = 8.8 Hz, 2H), 7.31 (d, J = 8.8 Hz, 2H). ^{13}C{^{1}H} NMR (126 MHz, chloroform-d): δ(ppm) = 36.4, 36.7, 116.1, 123.1, 129.2, 130.4, 150.0, 154.5.

ASSOCIATED CONTENT

Supporting Information. Electrochemical data, cartesian coordinates of calculated molecules, NMR spectra. “This material is available free of charge via the Internet at http://pubs.acs.org.”

AUTHOR INFORMATION

Corresponding Authors

Robert Francke - Institute of Chemistry, Rostock University, Albert-Einstein-Str. 3a, 18059 Rostock, Germany. E-mail: robert.francke@uni-rostock.de.
Michael Roemelt - Chair for Theoretical Chemistry, Ruhr-University Bochum, 44780 Bochum, Germany. E-Mail: michael.roemelt@theochem.ruhr-uni-bochum.de.

Authors

Arend F. Roesel - Institute of Chemistry, Rostock University, Albert-Einstein-Str. 3a, 18059 Rostock, Germany.
Mihkel Ugandi - Chair for Theoretical Chemistry, Ruhr-University Bochum, 44780 Bochum, Germany.
Nguyen Thi Thu Huyen - School of Chemical Engineering, Hanoi University of Science and Technology, 1 Dai Co Viet Road, Hanoi, Vietnam
Michal Májek - Department of Organic Chemistry, Faculty of Natural Sciences, Comenius University in Bratislava, Mlynská dolina, Ilkovičova 6, 84215 Bratislava, Slovakia.
Timo Broese - Institute of Chemistry, Rostock University, Albert-Einstein-Str. 3a, 18059 Rostock, Germany.

Author Contributions

The manuscript was written through contributions of all authors. All authors have given approval to the final version of the manuscript.

Notes

The authors declare no competing financial interest.

ACKNOWLEDGMENT

This work has been funded by the German Research Foundation (DFG, project no. FR 3848/3-1). MR and MU thank the DFG for funding through Emmy-Noether project RO 5688/1-1. Further financial support by the RoHan Project funded by the German Academic Exchange Service (DAAD, No. 57315854) and the Federal Ministry for Economic Cooperation and Development (BMZ) inside the framework "SDG Bilateral Graduate school program” is acknowledged. We thank Prof. Shannon S. Stahl (University of Wisconsin–Madison) for fruitful discussions during the 2020 Electrochemistry Gordon Research Conference. Furthermore, we thank Dr. Dirk Michalik and Dr. Jonas Bresien (both Rostock University, Institute of Chemistry) for carrying out NMR and Raman measurements.

REFERENCES

(1) Speiser, B.; Hammerich, O. *Organic Electrochemistry (5th edition)*; CRC Press Taylor & Francis Group: Boca Raton, 2016.

(2) Möhle, S.; Zirbes, M.; Rodrigo, E.; Gieshoff, T.; Wiebe, A.; Waldvogel, S. R. Modern Electrochemical Aspects for the Synthesis of Value-Added Organic Products. *Angew. Chem. Int. Ed.* **2018**, *57*, 6018–6041.

(3) Waldvogel, S. R.; Wiebe, A.; Gieshoff, T.; Möhle, S.; Rodrigo, E.; Zirbes, M. Electrifying Organic Synthesis. *Angew. Chem. Int. Ed.* **2018**, *57*, 5594–5619.

(4) Kärkäs, M. D. Electrochemical strategies for C-H functionalization and C-N bond formation: 5786-5865. *Chem. Soc. Rev.* **2018**, *47*, 5786–5865.

(5) Yan, M.; Kawamata, Y.; Baran, P. S. Synthetic Organic Electrochemical Methods Since 2000: On the Verge of a Renaissance. *Chem. Rev.* **2017**, *117*, 13230–13319.

(6) Xiong, P.; Xu, H.-C. Chemistry with Electrochemically Generated N-Centered Radicals. *Acc. Chem. Res.* **2019**, *52*, 3339–3350.

(7) Wang, P.; Gao, X.; Huang, P.; Lei, A. Recent Advances in Electrochemical Oxidative Cross-Coupling of Alkenes with H_2 Evolution. *ChemCatChem* **2020**, *12*, 27–40.

(8) Francke, R.; Little, D. Electrons and Holes as Catalysts in Organic Electrosynthesis. *ChemElectroChem* **2019**, *6*, 4373-4382.

(9) Costentin, C.; Savéant, J.-M. Concepts and tools for mechanism and selectivity analysis in synthetic organic electrochemistry. *Proc. Natl. Acad. Sci. USA* **2019**, *116*, 11147-11152.

(10) Okada, Y.; Yamaguchi, Y.; Ozaki, A.; Chiba, K. Aromatic “Redox Tag”-assisted Diels-Alder reactions by electrocatalysis. *Chem. Sci.* **2016**, *7*, 6387–6393.

(11) Imada, Y.; Okada, Y.; Chiba, K. Investigating radical cation chain processes in the electrocatalytic Diels-Alder reaction. *Beilstein J. Org. Chem.* **2018**, *14*, 642–647.

(12) Okada, Y.; Akaba, R.; Chiba, K. Electrocatalytic formal 2+2 cycloaddition reactions between anodically activated aliphatic enol ethers and unactivated olefins possessing an alkoxyphenyl group. *Org. Lett.* **2009**, *11*, 1033–1035.

(13) Yamamoto, T.; Riehl, B.; Naba, K.; Nakahara, K.; Wiebe, A.; Saitoh, T.; Waldvogel, S. R.; Einaga, Y. A solvent-directed

stereoselective and electrocatalytic synthesis of diisoeugenol. *Chem. Commun.* **2018**, *54*, 2771–2773.

(14) Park, Y. S.; Little, R. D. Redox electron-transfer reactions: Electrochemically mediated rearrangement, mechanism, and a total synthesis of daucene. *J. Org. Chem.* **2008**, *73*, 6807–6815.

(15) Broese, T.; Roesel, A. F.; Prudlik, A.; Francke, R. An Electrocatalytic Newman-Kwart-type Rearrangement. *Org. Lett.* **2018**, *20*, 7483–7487.

(16) Amatore, C.; Pinson, J.; Savéant, J. M.; Thiebault, A. Electron transfer induced reactions. Electrochemically stimulated aromatic nucleophilic substitution in organic solvents. *J. Am. Chem. Soc.* **1982**, *104*, 817–826.

(17) Pinson, J.; Savéant, J.-M. Electrolytic reduction of *p*-bromobenzophenone in the presence of benzenethiolate: an electrochemically catalysed aromatic nucleophilic substitution. *J. Chem. Soc., Chem. Commun.* **1974**, 933–934.

(18) Lloyd-Jones, G. C.; Moseley, J.; Renny, J. Mechanism and Application of the Newman-Kwart O→S Rearrangement of *O*-Aryl Thiocarbamates. *Synthesis* **2008**, 661–689.

(19) Newman, M. S.; Karnes, H. A. The Conversion of Phenols to Thiophenols via Dialkylthiocarbamates. *J. Org. Chem.* **1966**, *31*, 3980–3984.

(20) Zonta, C.; Lucchi, O. de; Volpicelli, R.; Cotarca, L. Thione-thiol rearrangement: Miyazaki-Newman-Kwart rearrangement and others. *Top. Curr. Chem.* **2007**, *275*, 131–161.

(21) Moseley, J. D.; Sankey, R. F.; Tang, O. N.; Gilday, J. P. The Newman–Kwart rearrangement re-evaluated by microwave synthesis. *Tetrahedron* **2006**, *62*, 4685–4689.

(22) Moseley, J. D.; Lenden, P. A high temperature investigation using microwave synthesis for electronically and sterically disfavoured substrates of the Newman–Kwart rearrangement. *Tetrahedron* **2007**, *63*, 4120–4125.

(23) Hoffmann, I.; Schatz, J. Microwave-mediated Newman–Kwart rearrangement in water. *RSC Adv.* **2016**, *6*, 80692–80699.

(24) Brooker, S.; Caygill, G. B.; Croucher, P. D.; Davidson, T. C.; Clive, D. L. J.; Magnuson, S. R.; Cramer, S. P.; Ralston, C. Y. Conversion of some substituted phenols to the corresponding masked thiophenols, synthesis of a dinickel(II) dithiolate macrocyclic complex and isolation of some metal- and ligand-based oxidation products. *J. Chem. Soc., Dalton Trans.* **2000**, 3113–3121.

(25) Harvey, J. N.; Jover, J.; Lloyd-Jones, G. C.; Moseley, J. D.; Murray, P.; Renny, J. S. The Newman–Kwart rearrangement of *O*-aryl thiocarbamates: Substantial reduction in reaction temperatures through palladium catalysis. *Angew. Chem., Int. Ed.* **2009**, *48*, 7612–7615.

(26) Perkowski, A. J.; Cruz, C. L.; Nicewicz, D. A. Ambient-Temperature Newman-Kwart Rearrangement Mediated by Organic Photoredox Catalysis. *J. Am. Chem. Soc.* **2015**, *137*, 15684–15687.

(27) The use of cerium ammonium nitrate in DMSO allows for reaction at room temperature, see Pedersen, S. K.; Ulfkjær, A.; Newman, M. N.; Yogarasa, S.; Petersen, A. U.; Sølling, T. I.; Pittelkow, M. Inverting the Selectivity of the Newman-Kwart Rearrangement via One Electron Oxidation at Room Temperature. *J. Org. Chem.* **2018**, *83*, 12000–12006.

(28) The Fe(II)/persulfate mediated NKR is carried out at temperatures between 45 and 65 °C, see Gendron, T.; Pereira, R.; Abdi, H. Y.; Witney, T. H.; Årstad, E. Iron(II)/Persulfate Mediated Newman-Kwart Rearrangement. *Org. Lett.* **2020**, *22*, 274–278.

(29) The increased rates are usually explained by a stabilization of the negative charge in Meisenheimer-type TS-1 by electron-withdrawing substituents (see ref. 18).

(30) Siu, J. C.; Fu, N.; Lin, S. Catalyzing Electrosynthesis: A Homogeneous Electrocatalytic Approach to Reaction Discovery. *Acc. Chem. Res.* **2020**, *53*, 547–560.

(31) Francke, R.; Little, R. D. Redox catalysis in organic electrosynthesis: Basic principles and recent developments. *Chem. Soc. Rev.* **2014**, *43*, 2492–2521.

(32) Nutting, J. E.; Rafiee, M.; Stahl, S. S. Tetramethylpiperidine *N*-Oxyl (TEMPO), Phthalimide N-Oxyl (PINO), and Related N-Oxyl Species: Electrochemical Properties and Their Use in Electrocatalytic Reactions. *Chem. Rev.* **2018**, *118*, 4834–4885.

(33) Savéant, J.-M. Molecular catalysis of electrochemical reactions. Mechanistic aspects. *Chem. Rev.* **2008**, *108*, 2348–2378.

(34) Ackermann, L. Metalla-electrocatalyzed C-H Activation by Earth-Abundant 3d Metals and Beyond. *Acc. Chem. Res.* **2020**, *53*, 84–104.

(35) The electron-catalyzed $S_{RN}1$-reactions (see refs. 16 and 17) constitute a particularly well studied system.

(36) In principle, another version of **TS-3** containing one *S*,*S*- and one *O*,*O*-acetal unit is also conceivable.

(37) Gilday, J. P.; Lenden, P.; Moseley, J. D.; Cox, B. G. The Newman-Kwart rearrangement: a microwave kinetic study. *J. Org. Chem.* **2008**, *73*, 3130–3134.

(38) Burns, M.; Lloyd-Jones, G. C.; Moseley, J. D.; Renny, J. S. The molecularity of the Newman-Kwart rearrangement. *J. Org. Chem.* **2010**, *75*, 6347–6353.

(39) Wang, J. *Analytical Electrochemistry (3rd Edition)*; Wiley-VCH, 2006.

(40) For further information see: https://www.gamry.com/digielch-electrochemical-simulation-software/.

(41) Chemical irreversibility of the $\mathbf{2t}/\mathbf{2t}^{\bullet+}$ couple was confirmed by lowering the upper vertex potential to 1.50 V (prior to the foot of the second wave). For more information, see the SI.

(42) Bard, A. J.; Faulkner, L. R. *Electrochemical Methods: Fundamentals and Applications*, 2. ed.; Wiley: New York, 2001.

(43) Hansch, C.; Leo, A.; Taft, R. W. A survey of Hammett substituent constants and resonance and field parameters. *Chem. Rev.* **1991**, *91*, 165–195.

(44) Francke, R.; Little, R. D. Optimizing electron transfer mediators based on arylimidazoles by ring fusion: synthesis, electrochemistry, and computational analysis of 2-aryl-1-methylphenanthro[9,10-*d*]dimidazoles. *J. Am. Chem. Soc.* **2014**, *136*, 427–435.

(45) Chiniforoush, S.; Cramer, C. J. Quantum Chemical Characterization of Factors Affecting the Neutral and Radical-Cation Newman-Kwart Reactions. *J. Org. Chem.* **2019**, *84*, 2148–2157.

(46) Cruz, C. L.; Nicewicz, D. A. Mechanistic Investigations into the Cation Radical Newman–Kwart Rearrangement. *ACS Catal.* **2019**, *9*, 3926–3935.

(47) Iffland, L.; Khedkar, A.; Petuker, A.; Lieb, M.; Wittkamp, F.; van Gastel, M.; Roemelt, M.; Apfel, U.-P. Solvent-Controlled CO_2 Reduction by a Triphos–Iron Hydride Complex. *Organometallics* **2019**, *38*, 289–299.

(48) Xue, G.; Geng, C.; Ye, S.; Fiedler, A. T.; Neese, F.; Que, L. Hydrogen-bonding effects on the reactivity of X-Fe(III)-O-Fe(IV)═O (X = OH, F) complexes toward C-H bond cleavage. *Inorg. Chem.* **2013**, *52*, 3976–3984.

(49) Cismesia, M. A.; Yoon, T. P. Characterizing Chain Processes in Visible Light Photoredox Catalysis. *Chem. Sci.* **2015**, *6*, 5426–5434.

(50) Ruccolo, S.; Qin, Y.; Schnedermann, C.; Nocera, D. G. General Strategy for Improving the Quantum Efficiency of Photoredox Hydroamidation Catalysis. *J. Am. Chem. Soc.* **2018**, *140*, 14926–14937.

(51) Streeter, I.; Wain, A. J.; Thompson, M.; Compton, R. G. In situ electrochemical ESR and voltammetric studies on the anodic oxidation of *para*-haloanilines in acetonitrile. *J. Phys. Chem. B* **2005**, *109*, 12636–12649.

(52) Andrieux, C. P.; Gallardo, I.; Junca, M. Mechanistic study of the electrochemical oxidation of some aromatic amines in the presence of bases. *J. Electroanal. Chem.* **1993**, *354*, 231–241.

(53) Schmidt, W.; Steckhan, E. Über organische Elektronenübertragersysteme, I. Elektrochemische und spektroskopische Untersuchung bromsubstituierter Triarylamin-Redoxsysteme. *Chem. Ber.* **1980**, *113*, 577–585.

(54) Francke, R.; Cericola, D.; Weingarth, D.; Kötz, R.; Waldvogel, S. R. Novel Electrolytes for Electrochemical Double Layer

Capacitors Based on 1,1,1,3,3,3-Hexafluoropropan-2-ol, *Electrochim. Acta* **2012**, 372-380.

(55) Colomer, I.; Chamberlain, A. E. R.; Haughey, M. B.; Donohoe, T. J. Hexafluoroisopropanol as a highly versatile solvent. *Nat. Rev. Chem.* **2017**, *1*, 0088.

(56) Pavlishchuk, V. V.; Addison, A. W. Conversion constants for redox potentials measured versus different reference electrodes in acetonitrile solutions at 25°C. *Inorg. Chim. Acta* **2000**, *298*, 97–102.

(57) Neese, F. Software update: the ORCA program system, version 4.0. *WIREs Comput Mol Sci* **2018**, *8*, 33.

(58) Chai, J.-D.; Head-Gordon, M. Long-range corrected hybrid density functionals with damped atom-atom dispersion corrections. *Phys. Chem. Chem. Phys.* **2008**, *10*, 6615–6620.

(59) Weigend, F.; Ahlrichs, R. Balanced basis sets of split valence, triple zeta valence and quadruple zeta valence quality for H to Rn: Design and assessment of accuracy. *Phys. Chem. Chem. Phys.* **2005**, *7*, 3297–3305.

(60) Grimme, S.; Antony, J.; Ehrlich, S.; Krieg, H. A consistent and accurate ab initio parametrization of density functional dispersion correction (DFT-D) for the 94 elements H-Pu. *J. Chem. Phys.* **2010**, *132*, 154104.

(61) Barone, V.; Cossi, M. Quantum Calculation of Molecular Energies and Energy Gradients in Solution by a Conductor Solvent Model. *J. Phys. Chem. A* **1998**, *102*, 1995–2001.

(62) Hong, D.-P.; Hoshino, M.; Kuboi, R.; Goto, Y. Clustering of Fluorine-Substituted Alcohols as a Factor Responsible for Their Marked Effects on Proteins and Peptides. *J. Am. Chem. Soc.* **1999**, *121*, 8427–8433.

(63) Neese, F.; Wennmohs, F.; Hansen, A. Efficient and accurate local approximations to coupled-electron pair approaches: An attempt to revive the pair natural orbital method. *J. Chem. Phys.* **2009**, *130*, 114108.

(64) Riplinger, C.; Sandhoefer, B.; Hansen, A.; Neese, F. Natural triple excitations in local coupled cluster calculations with pair natural orbitals. *J. Chem. Phys.* **2013**, *139*, 134101.

(65) Riplinger, C.; Neese, F. An efficient and near linear scaling pair natural orbital based local coupled cluster method. *J. Chem. Phys.* **2013**, *138*, 34106.

(66) Riplinger, C.; Pinski, P.; Becker, U.; Valeev, E. F.; Neese, F. Sparse maps—A systematic infrastructure for reduced-scaling electronic structure methods. II. Linear scaling domain-based pair natural orbital coupled cluster theory. *J. Chem. Phys.* **2016**, *144*, 24109.

(67) Truhlar, D. G. Basis-set extrapolation. *Chem. Phys. Lett.* **1998**, *294*, 45–48.

(68) Dunning, T. H. Gaussian basis sets for use in correlated molecular calculations. I. The atoms boron through neon and hydrogen. *J. Chem. Phys.* **1989**, *90*, 1007–1023.

(69) Woon, D. E.; Dunning, T. H. Gaussian basis sets for use in correlated molecular calculations. III. The atoms aluminum through argon. *J. Chem. Phys.* **1993**, *98*, 1358–1371.

(70) Balabanov, N. B.; Peterson, K. A. Systematically convergent basis sets for transition metals. I. All-electron correlation consistent basis sets for the 3d elements Sc-Zn. *J. Chem. Phys.* **2005**, *123*, 64107.

(71) Balabanov, N. B.; Peterson, K. A. Basis set limit electronic excitation energies, ionization potentials, and electron affinities for the 3d transition metal atoms: Coupled cluster and multireference methods. *J. Chem. Phys.* **2006**, *125*, 74110.

(72) Prascher, B. P.; Woon, D. E.; Peterson, K. A.; Dunning, T. H.; Wilson, A. K. Gaussian basis sets for use in correlated molecular calculations. VII. Valence, core-valence, and scalar relativistic basis sets for Li, Be, Na, and Mg. *Theor. Chem. Acc.* **2011**, *128*, 69–82.

(73) Dunlap, B. I.; Connolly, J. W. D.; Sabin, J. R. On some approximations in applications of Xα theory. *J. Chem. Phys.* **1979**, *71*, 3396.

(74) Vahtras, O.; Almlöf, J.; Feyereisen, M. W. Integral approximations for LCAO-SCF calculations. *Chem. Phys. Lett.* **1993**, *213*, 514–518.

(75) Weigend, F. Accurate Coulomb-fitting basis sets for H to Rn. *Phys. Chem. Chem. Phys.* **2006**, *8*, 1057–1065.

(76) Neese, F.; Wennmohs, F.; Hansen, A.; Becker, U. Efficient, approximate and parallel Hartree–Fock and hybrid DFT calculations. A 'chain-of-spheres' algorithm for the Hartree–Fock exchange. *Chem. Phys.* **2009**, *356*, 98–109.

(77) Izsák, R.; Neese, F.; Klopper, W. Robust fitting techniques in the chain of spheres approximation to the Fock exchange: The role of the complementary space. *J. Chem. Phys.* **2013**, *139*, 94111.

(78) Zhang, J.; Dolg, M. ABCluster: the artificial bee colony algorithm for cluster global optimization. *Phys. Chem. Chem. Phys.* **2015**, *17*, 24173–24181.

(79) Zhang, J.; Dolg, M. Global optimization of clusters of rigid molecules using the artificial bee colony algorithm. *Phys. Chem. Chem. Phys.* **2016**, *18*, 3003–3010.

(80) Grimme, S.; Bannwarth, C.; Shushkov, P. A Robust and Accurate Tight-Binding Quantum Chemical Method for Structures, Vibrational Frequencies, and Noncovalent Interactions of Large Molecular Systems Parametrized for All spd-Block Elements (Z = 1-86). *J. Chem. Theory Comput.* **2017**, *13*, 1989–2009.

(81) Grimme, S. Exploration of Chemical Compound, Conformer, and Reaction Space with Meta-Dynamics Simulations Based on Tight-Binding Quantum Chemical Calculations. *J. Chem. Theory Comput.* **2019**, *15*, 2847–2862.

(82) Brandenburg, J. G.; Bannwarth, C.; Hansen, A.; Grimme, S. B97-3c: A revised low-cost variant of the B97-D density functional method. *J. Chem. Phys.* **2018**, *148*, 64104.

(83) Kaji, A.; Araki, Y.; Miyazaki, K. Studies of the Thiocarbonyl Compounds. III. The Mechanism of the Thermal Rearrangement of Aryl Thionocarboxylates. *Bull. Chem. Soc. Jpn.* **1971**, *44*, 1393–1399.

(84) John, A.; Nicholas, K. M. Palladium Catalyzed C–H Functionalization of *O*-Arylcarbamates: Selective *ortho*-Bromination Using NBS. *J. Org. Chem.* **2012**, *77*, 5600–5605.

(85) Reddy, N. V.; Kumar, G. S.; Kumar, P. S.; Kantam, M. L.; Reddy, K. R.; Ligand-Assisted Copper-Catalyzed Oxidative Cross-Coupling of Simple Phenols with Formamides for the Synthesis of Carbamates. *Synlett* **2014**, *25*, 2133-2138.